



RESEARCH ARTICLE

10.1029/2023JD038874

Key Points:

- From an ice core in the southeastern Greenland ice sheet, we establish a time scale spanning 1799–2020 with a half-year uncertainty
- Over 221 years, the annual accumulation rate shows no significant trend, while the melt layer thickness has increased with Arctic warming
- The in-situ accumulation records provide an important basis for correcting reanalysis data, which in turn are valuable for improving models

Supporting Information:

Supporting Information may be found in the online version of this article.

Correspondence to:

K. Kawakami and Y. Iizuka,
kaoru@pop.lowtem.hokudai.ac.jp;
iizuka@lowtem.hokudai.ac.jp

Citation:

Kawakami, K., Iizuka, Y., Sasage, M., Matsumoto, M., Saito, T., Hori, A., et al. (2023). SE-Dome II ice core dating with half-year precision: Increasing melting events from 1799 to 2020 in southeastern Greenland. *Journal of Geophysical Research: Atmospheres*, 128, e2023JD038874. <https://doi.org/10.1029/2023JD038874>

Received 13 MAR 2023

Accepted 26 JUL 2023

Author Contributions:

Conceptualization: Kaoru Kawakami, Yoshinori Iizuka, Mahiro Sasage

Data curation: Kaoru Kawakami, Yoshinori Iizuka, Mahiro Sasage, Mai Matsumoto, Takeshi Saito, Keita Takasugi, Takumi Hatakeyama, Saaya Hamamoto, Akihisa Watari, Nao Esashi, Miu Otsuka, Shohei Hattori

SE-Dome II Ice Core Dating With Half-Year Precision: Increasing Melting Events From 1799 to 2020 in Southeastern Greenland

Kaoru Kawakami¹ , Yoshinori Iizuka¹ , Mahiro Sasage², Mai Matsumoto², Takeshi Saito¹, Akira Hori³ , Sakiko Ishino⁴ , Shuji Fujita^{5,6} , Koji Fujita⁷ , Keita Takasugi³, Takumi Hatakeyama⁸, Saaya Hamamoto⁷, Akihisa Watari², Nao Esashi⁷, Miu Otsuka², Ryu Uemura⁷ , Kazuho Horiuchi⁸ , Masahiro Minowa¹ , Shohei Hattori⁹ , Teruo Aoki⁵ , Motohiro Hirabayashi⁵, Kenji Kawamura^{5,6,10} , and Sumito Matoba¹ 

¹Institute of Low Temperature Science, Hokkaido University, Sapporo, Japan, ²Graduate School of Environmental Science, Hokkaido University, Sapporo, Japan, ³Kitami Institute of Technology, Kitami, Japan, ⁴Institute of Nature and Environmental Technology, Kanazawa University, Kanazawa, Japan, ⁵National Institute of Polar Research, Tokyo, Japan, ⁶Department of Polar Science, The Graduate University of Advanced Studies, SOKENDAI, Tokyo, Japan, ⁷Graduate School of Environmental Studies, Nagoya University, Nagoya, Japan, ⁸Hirosaki University, Hirosaki, Japan, ⁹International Center for Isotope Effects Research, School of Earth Sciences and Engineering, Nanjing University, Nanjing, China, ¹⁰Japan Agency for Marine Science and Technology, Yokosuka, Japan

Abstract Arctic warming has accelerated surface melting even in the highland areas of the Greenland ice sheet (GrIS). Understanding the relationship between climate and surface melting is essential for improving the estimates of ice-sheet mass loss due to warming. Here we analyze a 250 m-long ice core from the southeastern dome of GrIS (SE-Dome site; 67°19'17" N, 36°47'03" W, 3,161 m a.s.l.), where the annual mean temperature is −20.9°C and the accumulation rate is high and there is a large discrepancy among climate models regarding snow accumulation estimates. A time scale was established for 1799–2020 with a half-year uncertainty using annual counting of H₂O₂ concentration and five time horizons determined by electrical conductivity, melt events, and tritium concentration. The annual accumulation rate from the ice core shows no significant trend over 221 years and has an average of 1.04 ± 0.20 m w.e. year⁻¹. In contrast, the frequency and thickness of refrozen melt layer (ML) have increased over 221 years, and are synchronized with temperature changes in the Arctic. The thickness of MLs correlates positively with the time-integrated summer temperature anomaly using a reanalysis of air temperature. The in-situ accumulation records in the southeastern GrIS provide an important basis for correcting reanalysis data such as ERA5, which in turn are valuable for improving regional climate models.

Plain Language Summary In recent years, Arctic temperatures have been increasing faster than global temperatures. In the inland Greenland ice sheet (GrIS), the surface snow melts on warm days, then the meltwater percolates in the snowpack and refreezes into melt layers (MLs). Here we describe an ice core, collected from the southeastern GrIS, which contains records of precipitation and MLs from 1799 to 2020. We then compare these results with the climatic data. The annual precipitation rate obtained from the ice core shows neither a decrease nor an increase over 221 years, suggesting no significant trend in the southeastern region. On the other hand, with Arctic warming, the ML thickness per year has increased through the 19th–21st centuries. In addition, there is a positive correlation between ML thickness and summer temperature. We conclude that the annual precipitation rate in southeastern GrIS is constant regardless of Arctic warming and the ice core is favorable for reconstructing environmental records from the pre-industrial era to the present.

1. Introduction

Recent warming has accelerated surface melting, even in the highlands of the Greenland ice sheet (GrIS) (Otosaka et al., 2020; van den Broeke et al., 2016). Clarifying the relationship between temperature fluctuations and ice sheet melting from the pre-industrial era to the present is important for estimating ice sheet loss due to global warming. In the accumulation zone, the surface meltwater percolates through the snowpack and refreezes into melt features. Direct measurements of melt features involves analyzing ice cores to determine the melt-feature percentage (MFP), which is then used to reconstruct the history of surface melting (e.g., Fujita et al., 2021;

© 2023. The Authors.

This is an open access article under the terms of the [Creative Commons Attribution License](https://creativecommons.org/licenses/by/4.0/), which permits use, distribution and reproduction in any medium, provided the original work is properly cited.

Formal analysis: Kaoru Kawakami, Yoshinori Iizuka, Mahiro Sasage, Mai Matsumoto, Takeshi Saito, Akira Hori, Sakiko Ishino, Shuji Fujita, Masahiro Minowa, Shohei Hattori

Funding acquisition: Yoshinori Iizuka, Sakiko Ishino, Shohei Hattori, Teruo Aoki, Sumito Matoba

Investigation: Kaoru Kawakami, Yoshinori Iizuka, Mahiro Sasage, Mai Matsumoto, Akira Hori, Sakiko Ishino, Shuji Fujita, Koji Fujita, Ryu Uemura, Kazuho Horiuchi, Masahiro Minowa, Shohei Hattori, Sumito Matoba

Methodology: Akira Hori, Sakiko Ishino, Shuji Fujita, Koji Fujita, Masahiro Minowa, Shohei Hattori, Motohiro Hirabayashi, Kenji Kawamura

Project Administration: Yoshinori Iizuka

Validation: Kaoru Kawakami, Yoshinori Iizuka, Mahiro Sasage, Mai Matsumoto, Akira Hori, Sakiko Ishino, Shuji Fujita, Koji Fujita, Ryu Uemura, Kazuho Horiuchi, Shohei Hattori, Sumito Matoba

Visualization: Kaoru Kawakami, Sakiko Ishino, Masahiro Minowa

Writing – original draft: Kaoru Kawakami, Sakiko Ishino, Koji Fujita

Writing – review & editing: Yoshinori Iizuka, Akira Hori, Sakiko Ishino, Shuji Fujita, Koji Fujita, Ryu Uemura, Shohei Hattori, Teruo Aoki, Kenji Kawamura, Sumito Matoba

Graeter et al., 2018; Kameda et al., 1995). The number of melt features and their thickness has been increasing with recent warming (Kameda et al., 1995). After examining recent shallow ice cores from the percolation zone of western GrIS, Graeter et al. (2018) argued that a warming of 1.2°C in the summertime led to a near doubling of the MFP in 1995–2015 compared to the 1870–1900 time frame. Despite the need to better understand the relationship between climatic changes and surface melt from the pre-industrial era to the present, reconstruction of melt layer (ML) thickness over time is challenging because there can be a large uncertainty in the age of melt features (e.g., Westhoff et al., 2022).

Ice core time scales can be established via annual-layer counting, thanks to the seasonal cycles of some proxies, and constrained by events of known absolute age. Large-scale or high-latitude volcanic eruptions are recorded in ice cores as acid layers. They may be detected as peaks in either electrical conductivity and dielectric constant (Clausen et al., 1997; Hammer, 1980; Mojtavavi et al., 2020), or sulfate concentration peaks (Rasmussen et al., 2008) using ion chromatography. Nuclear materials originating from H-bomb tests, reaching their peak in 1963, have been recorded as tritium peaks and are particularly useful for anchoring the age of shallow ice cores (Qiao et al., 2021). For annual layer counting, seasonal variations in water isotope ratio and ion concentrations have been used to establish time scales for many ice cores (e.g., Sigl et al., 2016; Sinnl et al., 2022; Svensson et al., 2008). Hydrogen peroxide (H₂O₂) concentration is often used as a robust tool for annual layer counting because of its clear seasonality, which follows the annual insolation (e.g., Frey et al., 2006; Sigg & Neftel, 1988). However, in low accumulation sites where one desires to derive ice cores with long time records, H₂O₂ concentration in ice suffers from post-depositional effects such as remobilization in firn and decomposition by dust, which hampers precise dating by making its seasonal cycle unclear (Anklin et al., 1998; Gfeller et al., 2014). In contrast, Antarctic ice cores from high accumulation sites (>~0.3 m year⁻¹) have high H₂O₂ seasonal signals which are preserved over a few hundred years (Frey et al., 2006). In the GrIS, ice core drilling sites have accumulation rates of 0.23 m year⁻¹ in the Summit (Vinther et al., 2010), 0.22 m year⁻¹ in the NEEM (NEEM Community Members, 2013), and 0.12 m year⁻¹ in the EGRIP (Gerber et al., 2021). It is expected that ice cores from higher accumulation sites than Summit, NEEM, and EGRIP in the GrIS may be dated to the preindustrial period using H₂O₂ concentration.

A precise relationship between the age and depth of an ice core, while accounting for thinning and densification, helps provide basic climatic parameters such as accumulation rate at the drilling site (e.g., Miège et al., 2013). The accumulation rate on the GrIS has been studied using a variety of methods, including ice cores, snow-pit observations, meteorological station data, radar observations, and climate modeling. According to the accumulation map, which is based on estimates of accumulation rates from ice cores, snow pits, and weather stations in the various GrIS sites (Bales et al., 2009), the accumulation rate shows regional variations and increases from the northern to southern GrIS. Karlsson et al. (2020) conducted radar observations between the northern NGRIP and NEEM sites from 2007 to 2015 and reported accumulation rates of 0.11–0.26 m w.e. year⁻¹. Miège et al. (2013) also measured accumulation rates in the southern region using ice core data and reported a maximum accumulation rate of 1.26 m w.e. year⁻¹.

The models have also reconstructed accumulation rates in the GrIS. According to the Fifth Generation Mesoscale Model modified for polar climates (Polar MM5), firn cores, and meteorological station data, accumulation in the southeast is about 30% of the total accumulation in the GrIS (Burgess et al., 2010). Therefore, interannual variations of accumulation in this region strongly influence the surface mass balance of the entire GrIS (Burgess et al., 2010). The models have different approaches, and uncertainties about different spatial and temporal resolutions, different forcing fields, different ice sheet topographies and extents, etc. (Fettweis et al., 2020). Hence, Fettweis et al. (2020) aimed to improve on models' uncertainties by comparing different types of models, which are forced by the same ERA-Interim reanalysis forcing field. However, the discrepancies among the modeled snow accumulation rates are large, particularly in the southeast accumulation zone (2.0 m year⁻¹; Fettweis et al., 2020). The limited field observations of accumulation in the southeast make it difficult to assess accumulation rates and patterns with models such as regional climate models, and general circulation models (e.g., Fettweis et al., 2020). Therefore, detailed field observations of accumulation rates, particularly in the southeastern region, are needed.

Due to the high accumulation rate (1.02 ± 0.21 m w.e. year⁻¹) and seasonal accuracy in its time-scale (Furukawa et al., 2017), the southeast Dome (SE-Dome) ice core has the advantage of having minor post-depositional effects and high-resolution measurements of the aerosol species (Iizuka et al., 2018). However, a previously studied ice core drilled in 2015 (hereafter SE-Dome I ice core) was 90.45 m in length and contained environmental proxies

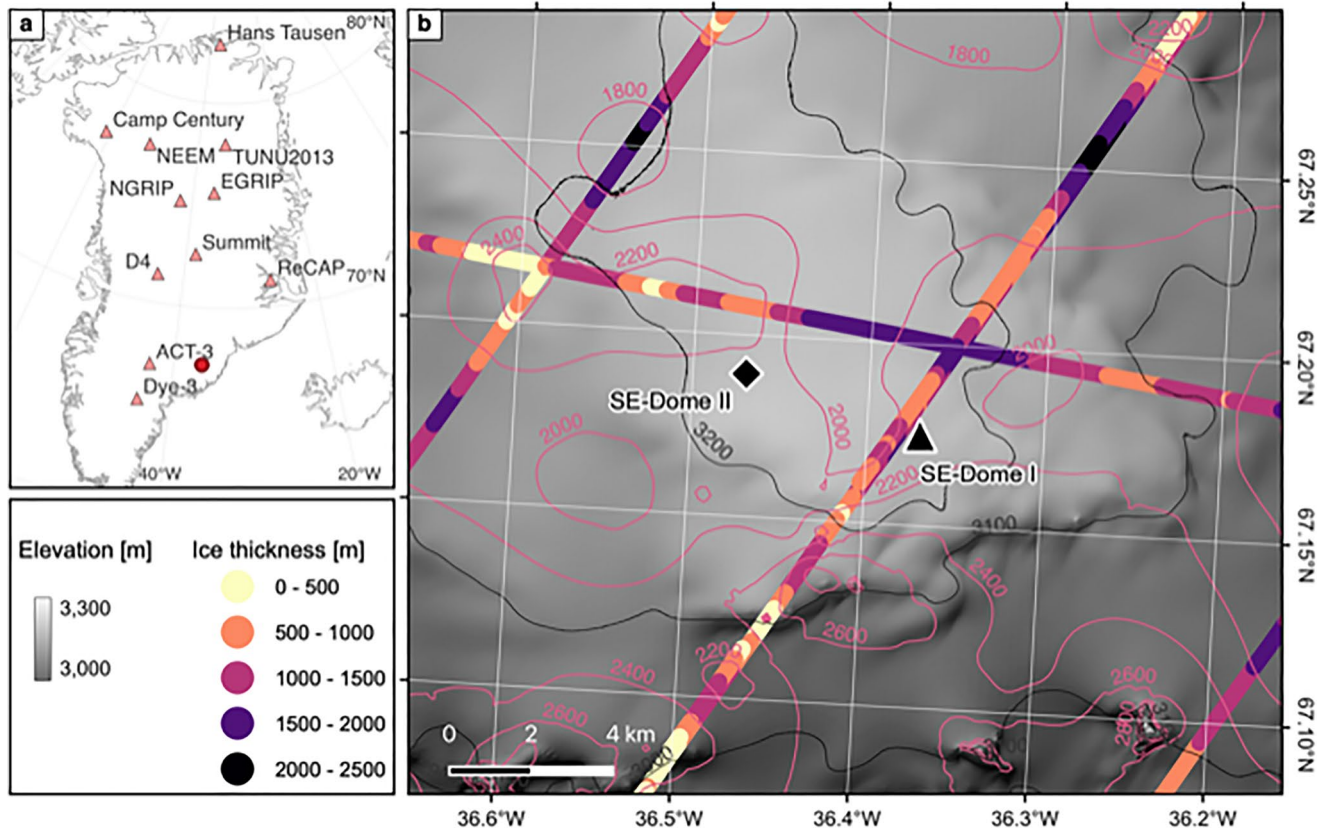


Figure 1. (a) The locations of the SE-Dome drilling site (red circle) and other ice core drilling sites (triangle) in Greenland ice sheet (GrIS). (b) The drilling site of SE-Dome I ice core (triangle, Iizuka et al., 2016) and SE-Dome II ice core (rhombus, Iizuka et al., 2021). Black and magenta solid lines indicate the surface and the bed elevations of the GrIS, respectively. The contour intervals are 100 m for the surface elevation and 200 m for the bed elevation. The ice surface elevation is based on ArcticDEM v3 (Porter et al., 2018). The bedrock topography is based on BedMachine v3 (Morlighem et al., 2017). The colored line indicates the ice thickness of the ice sheet obtained by airborne radar survey (IceBridge MCoRDS L2 Ice Thickness v1, Paden et al., 2010).

of only 60 years (Iizuka et al., 2018). To extend and add extremely high-resolution records, the work presented here recovered a much longer and older ice core 250 m in length (hereafter SE-Dome II ice core) in the same SE-Dome region (Iizuka et al., 2021).

In this study, we conducted physical, chemical, and optical measurements of the SE-Dome II ice core. The five time horizons were determined using electrical conductivity, melt events, tritium concentration, and the annual layers determined from the H_2O_2 data. Consequently, a time scale was established from 1799 to 2020 with a half-year uncertainty. We reconstructed the accumulation rate and ML thickness time series, compared it with reanalysis climatic data, and discussed the variations with Arctic warming.

2. Methods

2.1. SE-Dome II Ice Core

In spring 2021, a 250.79 m-long SE-Dome II ice core was drilled at SE-Dome in southeast GrIS (67°19'17" N, 36°47'03" W, 3,161 m a.s.l.; Figure 1). The details of the ice core drilling were described in Iizuka et al. (2021). The SE-Dome II ice core consisted of 552 sections, with an average section length of 0.45 m. The top depth of the SE-Dome II ice core is 1.27 m from the ice sheet surface. We conducted the following measurements, except for the tritium measurement (Section 2.5), at the Institute of Low Temperature Science, Hokkaido University, Japan. After melt feature observation (Section 2.2) and bulk density measurement (Section 2.3), longitudinal samples of 10 and 7 mm thickness were cut in the depth intervals, respectively, 1.27–88.80 m and 88.80–252.06 m, for the purpose of H_2O_2 measurements (Figure S1 in Supporting Information S1). Additional samples of 7 mm thickness were cut on the opposite side of the core in the depth interval 1.27–252.06 m, for measurements not relevant to

this report. We then microtomed its remaining core to obtain parallel flat surfaces by equalizing the thickness (average of about 75 mm) for analysis of physical properties. We decided that reducing the thickness of the H₂O₂ samples would not be a problem because the core reaches the close-off depth around 88.8 m. The average thickness of the 189 ice sections above 88.8 m is 74 mm, and 77 mm for the 363 sections below 88.8 m.

In Iizuka et al. (2021), the relationship between depth and age in the SE-Dome II ice core was estimated by the SEIS2016 age scale and annual accumulation rate (1.02 ± 0.21 m w.e. year⁻¹) from the SE-Dome I ice core (90.45 m depth; 1958–2014, Furukawa et al., 2017). Subsequently we estimated the four types of relationships between depth and age in the SE-Dome II ice core (Figure S2 in Supporting Information S1). Based on Figure S2 in Supporting Information S1, the bottom age of the SE-Dome II ice core falls within a range of 1783–1816.

In this study, water equivalent accumulation rate from the SE-Dome II ice core was obtained by correcting for the thinning due to ice flow with the Nye model (Paterson, 2006) and the estimated ice sheet thickness of 1,000 m (Figure 1), and using the annual average of high-resolution density as follows:

$$\text{Accumulation rate (m w.e. year}^{-1}\text{)} = \frac{1,000}{1,000 - h} * (d_s * \rho_s) \quad (1)$$

$$h = d_1 + \dots + d_{w-1}$$

$$d_w = d_s * \left(\frac{\rho_s}{\rho_w} \right)$$

where the d_s is annual layer thickness (m), d_w is water equivalent annual layer thickness (m w.e.), ρ_s is annual average density (kg m⁻³), ρ_w is water density (kg m⁻³) ($\approx 1,000$ kg m⁻³), and h is depth from the ice sheet surface (m w.e.). Based on this estimation, the bottom water equivalent depth of the SE-Dome II ice core falls at about 206 m, while the converted bottom depth is about 230 m. This results suggest that the thinning is approximately 10%. The annual layer thickness and converted annual layer thickness are described in Figure S3 in Supporting Information S1.

2.2. Observed Melt Features

Visual observations of melt features were conducted on the 552 sections under a light-emitting diode light with 920 lm (Elpa, ALT-1090IR(D)) in a cold room (−22°C). We divided the melt features into three types: (a) “melt layer (ML)” originating from a refrozen aquifer (Trusel et al., 2018; Figure S4a in Supporting Information S1) with more than 1 mm in thickness, (b) “percolated melt pipe (PMP)” consisting of refrozen meltwater during percolation without forming an aquifer (Figure S4b in Supporting Information S1) with more than 1 mm in thickness (Pfeffer & Humphrey, 1998), and (c) “melt crust (MC)” with 1 mm or less in thickness (Figure S4c in Supporting Information S1). The MCs probably originate in snowpack crusts (e.g., Fegyveresi et al., 2018; Weinhart et al., 2021). Crusts are commonly high density and can be formed in different environmental conditions: for example, long sunshine duration, high temperature, strong wind, low relative humidity, and high accumulation (e.g., Weinhart et al., 2021).

To investigate how large a melt event was, the melt feature percentage (MFP %) was calculated with an ice density of 900 kg m⁻³ (Kameda et al., 1995) as follows:

$$\text{MFP} = \frac{900 * d_m}{900 * d_m + \rho_f * d_f} * 100 \quad (2)$$

where d_m and d_f are melt features thickness and firn layer thickness in annual layer thickness, and ρ_f is annual average density in the annual firn layer.

2.3. Density Measurements

We measured bulk density of whole sections by measuring the weight and size of the cores (volumetric method). In addition, a continuous density profile on a microtomed section was obtained using the X-ray transmission method (Hori et al., 1999). In this method, the intensity of X-rays transmitted through a core sample was continuously measured using an X-ray detector during the translation of the sample across the

beam. The X-ray intensity profile was then converted into a density profile using a calibration curve of X-ray intensities as a function of the thickness of pure ice. The spatial resolution of the density profile was approximately 1 mm.

2.4. Continuous Dielectric Profile (DEP)

To detect volcanic events, electrical conductivity was measured on whole sections using the continuous dielectric profile method (Moore & Paren, 1987; Wilhelms et al., 1998) at an average temperature of -22°C . This method produced a profile of electrical conductivity at 250 kHz and provided the signal of the acid content (Wolff, 2000). The analytical resolution was 20 mm.

2.5. Tritium Measurements

The tritium content was determined using a liquid scintillation counter (LSC-LB3, Aloka Co. Ltd.). From Figure S1 in Supporting Information S1, 24 samples from 76.831 to 89.750 m in depth were measured to detect the depth corresponding to 1963 at the National Institute of Polar Research (NIPR), Japan. The average resolution of the samples was 565 mm, corresponding to a half-year time resolution.

2.6. H_2O_2 Concentration Measurements and Dating of the Ice Core

Samples of 7 or 10 mm thickness were measured for H_2O_2 concentrations at depth resolutions of 3–7 cm (Figure S1 in Supporting Information S1). The total was 4,968 samples, covering the entire SE-Dome II ice core. The samples were put into pre-cleaned 15 mL tubes and melted at room temperature ($+25^{\circ}\text{C}$). H_2O_2 concentrations were determined by the fluorometric method following Lazrus et al. (1985). Briefly, the samples are carried by peristaltic pump to the continuous flow system, where the fluorescent dimer is produced via a reaction of H_2O_2 with 4-ethylphenol catalyzed by the presence of the enzyme peroxidase, and detected by the fluorescent detector (Jasco, FP-4025) at excitation and emission wavelengths of 326 and 410 nm, respectively, at $\text{pH} > 12$. The uncertainty was estimated by replicate analyses of 20 sets of standards ranging from 0 to $350 \mu\text{g kg}^{-1}$, used to calibrate 140 samples in a measurement day. The uncertainties varied, depending on the concentration of standards, showing ± 2.1 and $\pm 7.4 \mu\text{g kg}^{-1}$ for 8.75 and $350 \mu\text{g kg}^{-1}$ standards, respectively. Absolute concentration of the liquid H_2O_2 standard was determined by titration with KMnO_4 at the beginning and the end of the 3 month measurement period which showed little decay (within 5%). The SE-Dome II ice core is half-annually dated by assuming that minima and maxima in H_2O_2 concentration correspond to mid-winter and mid-summer, respectively (see Supporting Information S1).

2.7. ERA5 Reanalysis Climate Data

We used the ERA5 reanalysis data sets distributed by the European Center for Medium-Range Weather Forecasts (Hersbach et al., 2020) to compare climate records with the SE-Dome II ice core (1950–present). We extracted the hourly air temperature at the SE-Dome site (T_{PL} , $^{\circ}\text{C}$) from the hourly pressure level temperatures (T_p and T_{p+1} , $^{\circ}\text{C}$) at the closest geopotential heights (z_p and z_{p+1} , m a.s.l.) including the site elevation (z_{site} , m a.s.l.) as:

$$T_{\text{PL}} = \frac{T_{p+1} - T_p}{z_{p+1} - z_p} (z_{\text{site}} - z_p) + T_p \quad (3)$$

where p is a pressure level that satisfies $z_p \leq z_{\text{site}} < z_{p+1}$ (Khalzan et al., 2022; Sakai et al., 2015). With the hourly air temperature (T_{PL} , $^{\circ}\text{C}$), we calculated a positive degree hour sum (PDH, $^{\circ}\text{C h}$) in summer (June, July, and August) of each year as:

$$\text{PDH} = \sum \max[0, (T_{\text{PL}} - T_T)] \quad (4)$$

where T_T is a threshold temperature ($^{\circ}\text{C}$) because the snow melting could occur even below 0°C , and the ERA5 based temperature could have a certain bias. We changed the threshold temperature from -8 to 0°C at a 0.5°C interval, and then obtained a correlation coefficient with the melt feature thickness between 1950 and 2020 for each threshold temperature (Section 3.3).

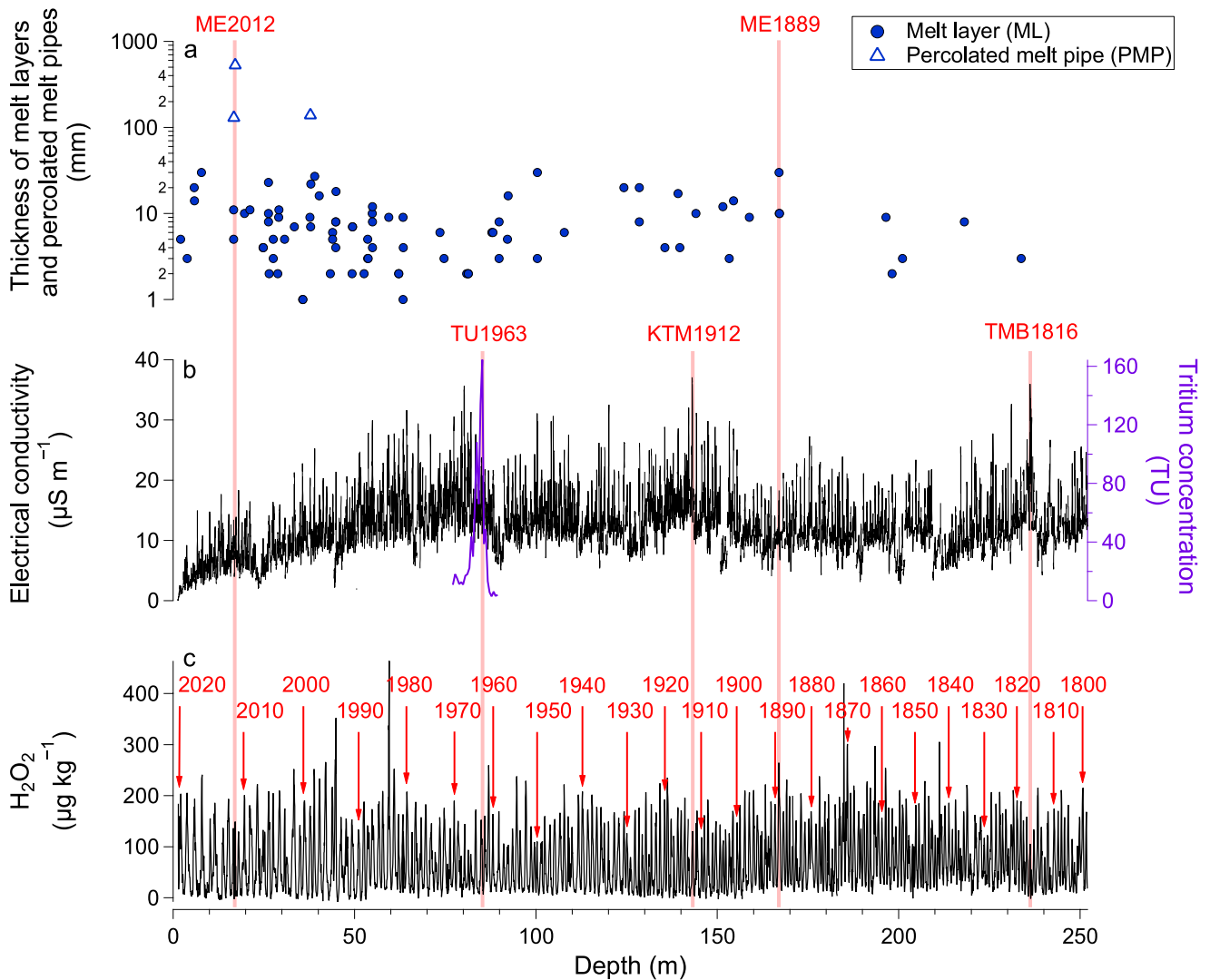


Figure 2. Depth profiles of several proxies in the SE-Dome II ice core. (a) Thickness of melt layers, and percolated melt pipes (mm); (b) electrical conductivity ($\mu\text{S m}^{-1}$) and tritium concentration (TU) from 76.831 to 89.750 m in depth; (c) H_2O_2 concentration ($\mu\text{g kg}^{-1}$). “ME2012,” “ME1889,” “TU1963,” “KTM1912,” and “TMB1816” indicate time markers from melting events in 2012 and 1889, the tritium peak in 1963, and the volcanic eruptions of Katmai 1912 CE and Tambora 1816 CE.

3. Results and Discussion

3.1. Core Chronology

Figure 2 shows melt events, the tritium peak, and volcanic events in the SE-Dome II ice core. We observed 86 MLs in the ice core. The PMPs are observed above ~ 38 m, at 16.693–16.823 m (130 mm in thickness), 16.826–17.356 m (530 mm in thickness), and 37.784–37.922 m (138 mm in thickness). An extreme melt event was found between 16.652 and 17.356 m including two MLs of 11 and 5 mm in thickness, as well as two PMPs of 130 and 530 mm in thickness (Figure 2a). Such thick PMPs are only observed between 16.693 and 17.356 m, suggesting the events in the core are due to an extreme surface melting event in 2012 (Nghiem et al., 2012; “ME2012” in Figure 2a). In the deeper core section, a ML of 30 mm thickness was observed at ~ 167.024 – 167.054 m depth. This is the only thick ML below 150 m, and the interval corresponds to 1886–1889 CE, as determined from the previous estimation of relationships between depth and age in the SE-Dome II ice core (Iizuka et al., 2021, and some additional consideration as in Figure S2 in Supporting Information S1). Hence, this thick ML is identified as the 1889 melting event in widely found in GrIS ice cores (e.g., Neff et al., 2014; “ME1889” in Figure 2a). The time horizon in 1963 is determined by the tritium peak originating from the H-bomb test. A sharp tritium peak was found at 84.928–85.469 m depth (“TU1963” in Figure 2b), accounting for the H-bomb test in 1963 (Clausen & Hammer, 1988).

Figure 2b also shows the depth profile of electrical conductivity. The baseline increases to ~80 m depth and then shows no change to the bottom of the ice core. The electrical conductivity has a peak at the depth with high acid concentration, implying volcanic events or high emission of anthropogenic substances. The two highest peaks ($\geq 35.9 \mu\text{S m}^{-1}$) were found at 143.07 and 236.22 m, corresponding to the periods 1907–1918 and 1800–1830 based on estimated relationships between depth and age shown in Figure S2 in Supporting Information S1. Following volcanic chronologies of the NEEM ice core and the Humboldt ice core in northern GrIS (e.g., Sigl et al., 2013), the peaks at 143.07 and 236.22 m were interpreted to correspond to deposited acidic materials in 1912 and 1816 from the colossal eruptions of Katmai (Volcanic Explosivity Index [VEI] > 6) in 1912 (“KTM1912” in Figure 2b) and Tambora (VEI > 7) in 1815 (“TMB1816” in Figure 2b). In summary, five time horizons were detected, corresponding to 2012, 1963, 1912, 1889, and 1816 in the SE-Dome II ice core.

Figure 2c and Figure S6 in Supporting Information S1 show the depth profile of H_2O_2 concentration. The average concentration is $71.0 \pm 58.5 \mu\text{g kg}^{-1}$. Three authors (S.I., Y.I., and S.H.) counted local minima and maxima of H_2O_2 and estimated annual layers. The layer counting of the H_2O_2 data revealed that the 250.79 m-long SE-Dome II ice core covers the period between 1799 and 2020 (Figure 2c and Figure S6 in Supporting Information S1). The annual layers are consistent with the five time horizons (2012, 1963, 1912, 1889, and 1816) (light pink lines in Figure 2), validating the accuracy of our layer counting. Thus, the ice-core time scale (SE2time2023) established here with an uncertainty better than a year, provides an important basis for precise reconstruction of the histories of climate and aerosols for the industrial period (221 years, from 1799 to 2020).

It should be noted that the seasonal cycle in H_2O_2 concentration can be gradually smoothed due to evaporation, diffusion, and recondensation within firn as has long been discussed (e.g., Mosley-Thompson et al., 2001), possibly varying the timing of the minimum and maximum. For ice cores collected around NEEM, northwest GrIS, Gfeller et al. (2014) assigned the H_2O_2 minimum to January and maximum to July based on the fact that H_2O_2 winter minima lead $\delta^{18}\text{O}$ by about a month (Mosley-Thompson et al., 2001) with the $\delta^{18}\text{O}$ seasonality determined for NEEM (Steen-Larsen et al., 2011). On the other hand, for a shallow core at Dye-3, which is located in the southern GrIS relatively close to SE-Dome, Sigg and Neftel (1988) showed that H_2O_2 maxima are later than that of $\delta^{18}\text{O}$, possibly suggesting the shift of H_2O_2 peaks after deposition. However, the post-depositional change in H_2O_2 at SE-Dome is expected to be less significant than that at Dye-3, owing to its better preservation of H_2O_2 due to a higher accumulation rate ($> 1 \text{ m w.e. year}^{-1}$ compared to $\sim 0.5 \text{ m w.e. year}^{-1}$ (Buchardt et al., 2012)) and slightly colder temperature (-21°C (Iizuka et al., 2017) compared to -19.6°C (Sigg & Neftel, 1988)). This is supported by the analysis of H_2O_2 in multiple ice cores in West Antarctica by Frey et al. (2006) who showed that the post-depositional loss of H_2O_2 tends to be smaller in sites with higher accumulation and lower temperature. We therefore do not consider the shift of H_2O_2 peaks for the SE-Dome II ice core in the present work.

Surface melting and a high amount of impurities may decrease the H_2O_2 concentrations in snowpack (Anklin et al., 1998). Thus, extreme melting and high impurity content by volcanic eruptions may affect the H_2O_2 records in the SE-Dome II ice core. For example, the collapsed peak at 143.07 and 236.22 m corresponding to 1912 and 1816 are determined due to the large eruptions of Mt. Katmai and Tambora. The low or collapsed peaks provide excellent opportunities for age validation. The low H_2O_2 concentration around 13.021 m corresponding to 2014, which coincides with high volcanic impurity flux in the autumn of 2014 from the eruption of Mt. Bardarbunga in Iceland (Amino et al., 2021) (VEI = 0; Figure S6a in Supporting Information S1). The collapsed H_2O_2 peak around 16.770 m dates to 2012, which is well known for the extreme melt event (Nghiem et al., 2012; Figure S6b in Supporting Information S1). The low H_2O_2 peak at 31.266 m dates to 2003 (Figure S6c in Supporting Information S1), which was reported to be characterized by high dust concentration in the summer (Amino et al., 2021). The collapsed peaks at 217.170 and 219.720 m correspond to 1836 and 1833 with the large eruption of Mt. Cosigüina in Nicaragua (VEI > 5; Kohno & Fujii, 2002, Figure S6d in Supporting Information S1) and Mt. Babuyan in Philippine (VEI > 4; Sigl et al., 2013, Figure S6e in Supporting Information S1). Consequently, these characteristic layers with markedly low H_2O_2 peaks even in the deeper part of the ice core are fully explainable with the known events according to our chronology, thus supporting its high reliability. We conclude that the maximum uncertainty of our timescale is smaller than 0.5 years as it is constrained biannually.

We then compared our time scale (SE2time2023) with the GrIS ice-core chronology GICC21 (Sinnl et al., 2022). In Figure S7 in Supporting Information S1, the electrical conductivities of NGRIP, EGRIP, and SE-Dome II ice core are presented. GICC21 uses two volcanic tie-points with known event dates during 1800–2020: the 1912 Katmai eruption and the 1816 Tambora eruption. For these volcanic tie points, SE2time2023 is considered

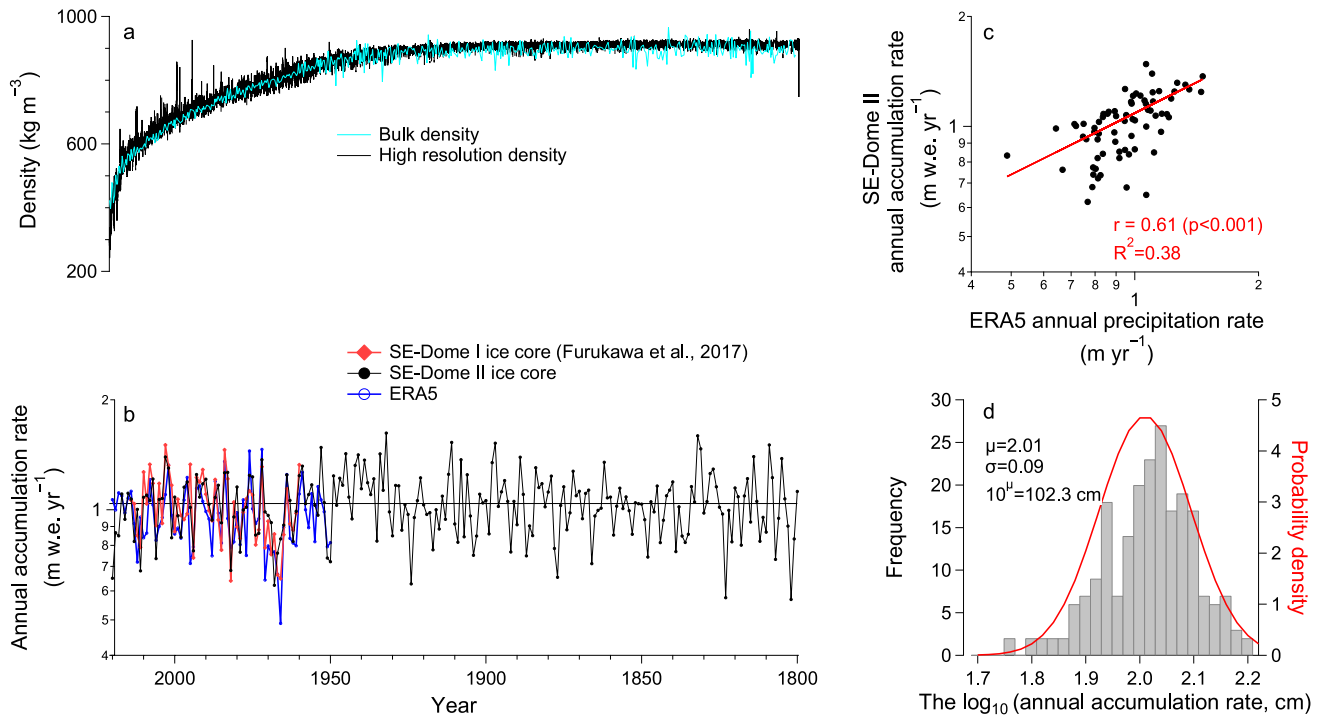


Figure 3. Time series of several proxies in the SE-Dome II ice core. (a) Bulk density (kg m^{-3}) and high-resolution density (kg m^{-3}), (b) accumulation rate (m w.e. year^{-1}) from the SE-Dome II ice core and SE-Dome I ice core (Furukawa et al., 2017), and precipitation rate (m year^{-1}) from ERA5 data, (c) the relationship between the annual precipitation rate from ERA5 and the annual accumulation rate from the SE-Dome II ice core from 1950 to 2020, (d) the distribution of converted annual layer thicknesses (annual accumulation rate).

consistent with GICC21. Turning to other volcanic signal peaks, the 1894 peak is detected in the EGRIP (northern Greenland) but not in the NGRIP and SE-Dome II ice core (central and southern Greenland). The 1833 Babuyan eruption signal is detected in both EGRIP and SE-Dome II ice core. In contrast, the 1836 Cosiguina eruption signal is detected at all sites. The SE-Dome and other ice cores (NGRIP and EGRIP) agree in age within a year. Sinnl et al. (2022) noted that GICC21 has a dating error of 1 year per century due to its ability to go back into the much farther past ($\sim 3,800$ years). The age agreement between the cores suggests that the GICC21 timescale is precise within a year in recent years from 1816.

3.2. Density and Snow Accumulation Rate Reconstructed From the SE-Dome II Ice Core

The bulk density is 423 kg m^{-3} at the top section (1.27–1.76 m) and increases with depth (Figure 3a). At about 88 m, the typical close-off density of 830 kg m^{-3} is reached. Deeper than the close-off depth, the bulk density still increases with bubble compression and finally reaches 900 kg m^{-3} . Figure 3a also shows the profile of high-resolution density. As with the bulk density, the high-resolution density increases with depth and reaches 830 kg m^{-3} at 88.9 m. In the deeper part of the ice core, the high-resolution density converges to 917 kg m^{-3} with much less variability than the bulk density. The high-resolution density profile shows high peaks that correspond to visually observed MLs and PMPs (Figure 2a). The high-resolution density profile of the SE-Dome II ice core is similar to that of the SE-Dome I ice core (Iizuka et al., 2017) as expected from their proximity. For example, the close-off density reaches 86.8 m depth in the SE-Dome I ice core, and 88.9 m for the SE-Dome II ice core.

Figure 3b shows that the result indicates that the maximum and minimum annual accumulation rates of 1.62 and $0.57 \text{ m w.e. year}^{-1}$ occurred in 1932 and 1802, respectively. According to the nonparametric Mann-Kendall test for monotonic trends (Kendall, 1975; Mann, 1945), the annual accumulation rate over the past 221 years shows no significant temporal trend (Figure 3b). Although the ice sheet thickness was estimated as 1,000 m (Section 2.1), we confirmed that the different ice sheet thicknesses in the Nye model (750 and 1,250 m) did not affect the result of no temporal trend in accumulation rates. The average annual accumulation rate between 1800 and 2020 is $1.04 \pm 0.20 \text{ m w.e. year}^{-1}$. The SE-Dome II annual accumulation rates between 1960 and 2014 are in good

agreement with the SE-Dome I ice core with the SEIS2016 age scale (1.02 ± 0.21 m w.e. year⁻¹ during 1960–2014; Furukawa et al., 2017; Figure 3b), supporting the robustness of our result. According to the precipitation rates based on the compiled data of GrIS ice cores (Mernild et al., 2015), the precipitation rates from the Summit ice core and TUNU2013 ice core in central-east and northeastern GrIS also show no significant trend between 1890 and 2000. In contrast, in the precipitation rates from the ACT-11d ice core in the southwestern region, an increase in precipitation rate between 1890 and 2000 is observed (Mernild et al., 2015). These results suggest that the trend of annual accumulation rate in the SE-Dome site is similar to that in the northeastern and central-east GrIS. This indicates that there are differences in the accumulation rate trends between the western and eastern regions of the southern GrIS. The differences are likely due to the fact that the eastern region is prone to climate systems such as prevailing easterly winds and frequent cyclogenesis over eastern GrIS (Hanna et al., 2006).

We then compare the annual accumulation rate of the SE-Dome II ice core and precipitation rates from ERA5 showing an average of 0.96 ± 0.19 m year⁻¹ between 1950 and 2020 (Figure 3b). Figure 3c shows the relationship between the precipitation rate data from ERA5 and the annual accumulation rate from the SE-Dome II ice core between 1950 and 2020. The correlation coefficient is significantly positive in 1950–2020 ($r = 0.61$, $R^2 = 0.38$, $p < 0.001$; Figure 3c). The slope of the regression line is 0.62, indicating that the ERA5 reanalysis data has a small underestimation compared to the accumulation rates estimated from the SE-Dome II ice core.

In GrIS ice cores, the annual layer thicknesses tend to be distributed lognormally (e.g., Andersen et al., 2006). The annual accumulation rate (annual layer thickness) from the SE-Dome II ice core is also lognormally distributed (Figure 3d), suggesting that snow accumulation in the SE-Dome has been deposited homogeneously within a statistical order for the past 221 years with very little frequency of extremely low or high accumulation due to special events. The result being statistically homogeneous with very few anomalies in the annual accumulation rate is probably a characteristic of southeastern Greenland, and this may lead to reduced uncertainty in snow accumulation rate from modeling studies (Fettweis et al., 2020).

3.3. Relationship Between the Melt Layer Thickness and Arctic Summer Warming

In the Arctic, temporal warming has occurred starting in the 1920s (Chylek et al., 2006). Subsequently, the Arctic temperature declined around 1970, warmed in the 1980s (Aizawa et al., 2022), followed by more warming into the present (Serreze & Francis, 2006). According to ice core studies, the recent temperatures in north and central GrIS are on average $1.5 \pm 0.4^\circ\text{C}$ higher than in the twentieth century (Hörhold et al., 2023). To investigate the temperature changes in the southeastern GrIS, in this section, we focus on the record of melt features from the SE-Dome II ice core to reconstruct summer air temperature. As described in Section 2.2, the melt features are divided into three types: MLs, PMPs, and MCs. In the following, we begin by investigating the characteristics of MCs and comparing them with other regions of the GrIS.

During the period spanning 1800–2020, the number of MCs is 355 (Figure 4a). Based on a decadal sum, the frequency of MCs has increased markedly from 8.0 ± 3.2 per decade before 1920, to 25.9 ± 5.4 per decade after 1920. The MCs can be formed by various mechanisms such as strong wind, high temperature, and high accumulation (e.g., Fegyveresi et al., 2018; Weinhart et al., 2021). The increase of MCs after 1920 might be due to minor surface melting on warm days, because the 1920s was a strongly warming decade (Chylek et al., 2006). Weinhart et al. (2021) suggest that there is a positive correlation ($R^2 = 0.89$) between the logarithmic accumulation rate and MC numbers per annual layer in the surface snow of both Antarctica and northern Greenland. They concluded that the formation of MCs is directly related to the number of snow deposition events per year. However, the annual number of MCs and accumulation rate at the SE-Dome site does not show a significant correlation ($r = 0.13$, $p = 0.06$; Figure S8 in Supporting Information S1). This result suggests that the formation mechanisms of MCs in the SE-Dome ice core, where there is a high annual accumulation rate (1.04 m w.e. year⁻¹), may be different from the northern GrIS. There is only one ice core data of sufficiently high accumulation (>0.5 m w.e. year⁻¹) in the southeastern region, so we are unable to demonstrate a reason for the lack of correlation between the annual number of MCs and the accumulation rate. Further study is needed about the number of MCs in various regions of the GrIS.

ML thickness is a proxy for the amount of refrozen meltwater (Trusel et al., 2018). In the case of PMP, the amount of refrozen meltwater was estimated as follows. The positive anomaly in high-resolution density for the PMP relative to the neighboring depths should reflect the amount of percolated meltwater. We calculated the residuals

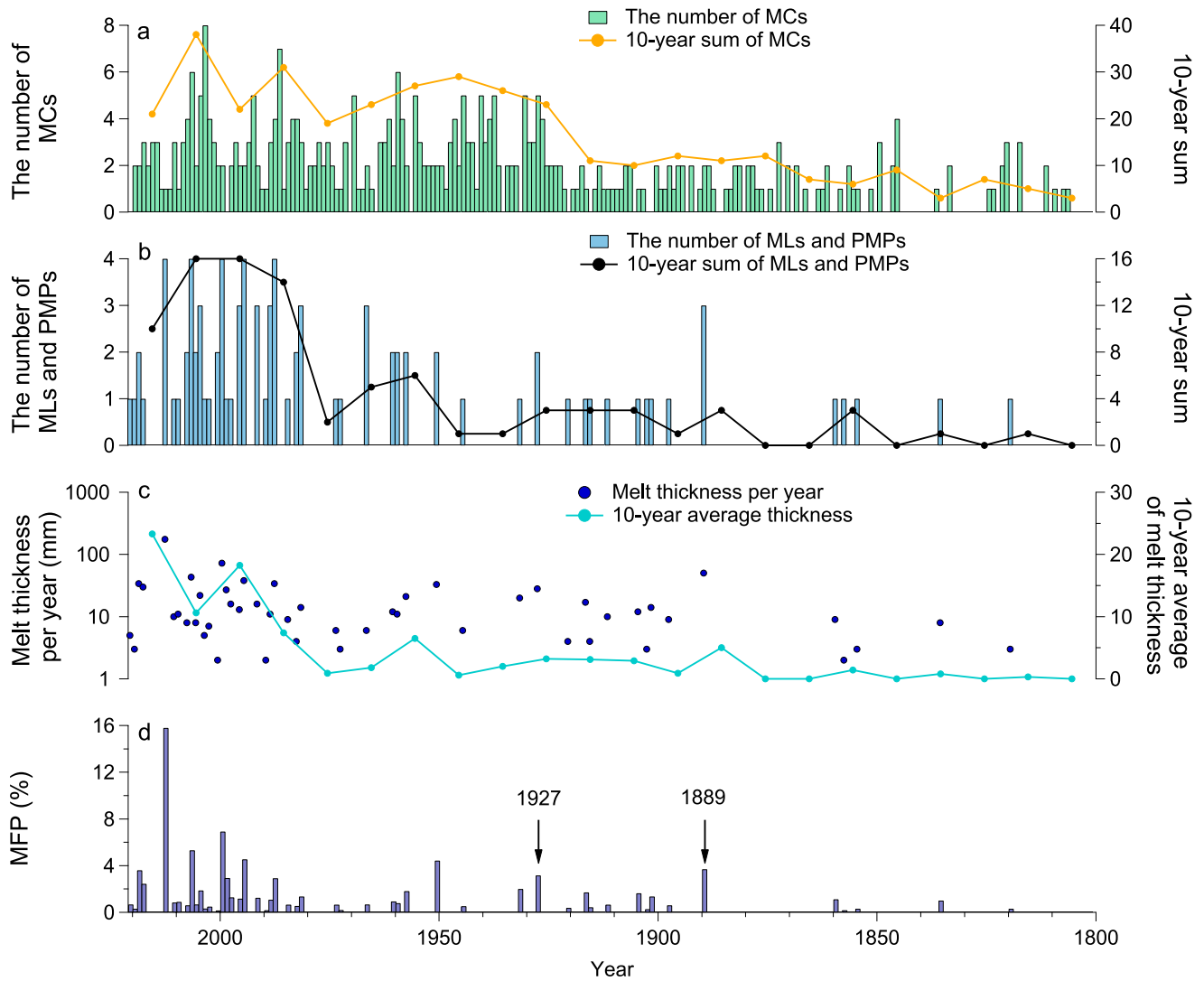


Figure 4. The age profiles of melt features. (a) The number of melt crusts (MCs) per year and the 10-year sum number of MCs, (b) the number per year and 10-year sum number of melt layers and percolated melt pipes, (c) melt thickness per year and 10-year average thickness and (d) melt feature percentage per year (MFP) between 1800 and 2020.

of the density of the PMP and the nearest ML relative to those of the 1-m average around the PMP and the ML. Then the ratio of the PMP density residual to that of the ML was obtained. This ratio enables us to convert the length of the PMP to the equivalent length of the ML. By this estimation, the ML equivalent thicknesses are 31.20 and 127.20 mm for 2012, and 34.50 mm for 1999. Based on this estimation, we use the ML thickness including the equivalent thicknesses of PMPs, as an indicator of the melt amount in the summer.

We then focused on the frequency and thickness of MLs and PMPs. Figure 4b shows the frequency of MLs including PMPs per year and its 10-year sum. The frequency has increased remarkably from 0.18 per year before 1980, to 1.40 per year after 1980. Based on the nonparametric Mann-Kendall test for monotonic trends (Kendall, 1975; Mann, 1945), the 10-year sum of melt frequency shows a statistically significant increasing trend ($p < 0.001$, Figure 4b). Although the ongoing Arctic warming first started in the 1970s (Aizawa et al., 2022), our results suggest that the warming in recent decades began in the 1980s, creating an environment likely to form a ML at the SE-Dome site. Figure 4c shows the melt thickness per year between 1800 and 2020 in the SE-Dome II ice core, including the ML thickness and the thickness equivalents of the PMPs. Note that the thickness of MCs per year does not affect the trend of melt thickness because the melt thickness has 1–100 mm order while the average thickness of MCs per year is 1.61 mm. The average melt thicknesses per decade decreased in cold periods

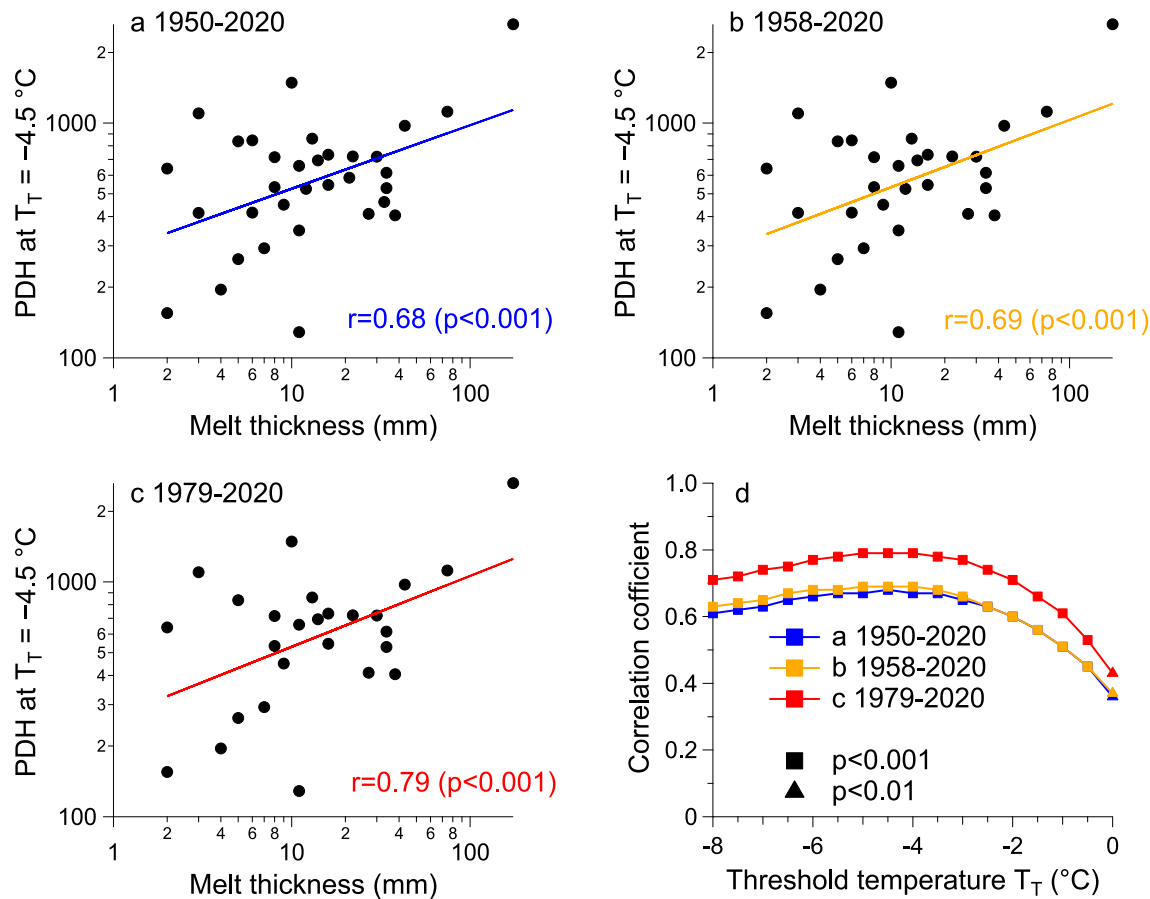


Figure 5. Scatter plot of melt thickness and positive degree hour sum (PDH) with $T_T = -4.5^\circ\text{C}$ during three periods: (a) 1950–2020, (b) 1958–2020, and (c) 1979–2020. (d) The correlation coefficient between melt thickness and PDH ($^\circ\text{C h}$) given by threshold temperature (T_T , $^\circ\text{C}$) from -8.0 to 0°C during three periods. Both melt thickness and PDH are presented on a logarithmic scale due to the large variability.

during the 1960s with 1.80 mm thickness, then increased since the 1980s with 14.89 mm thickness per decade (Figure 4c). We did the nonparametric Mann-Kendall test with 10-year average thickness and the melt thicknesses show a statistically significant increasing trend ($p < 0.001$, Figure 4c). Both the decadal melt frequency and melt thickness have increased, however, the frequency declined while the thickness increased from the 2000s to the 2010s. This result suggests that the amount of melting at one time has increased since 2000. In summary, the melt frequency and melt thickness have been increasing at the SE-Dome site. The frequency has increased since the 1980s, suggesting that the warming at the SE-Dome site started in the 1980s. Also, each melting event has been more likely to form a thick ML since 2000.

We also investigated the relationship between the melt thickness per year, including the ML thicknesses and the equivalent thicknesses of PMPs, and the summer temperature (June, July, and August) using ERA5 data at the SE-Dome site. ERA5 data has been quality-assured from 1979 to present, and recently the period from 1958 to 1978 was also quality-assured. We changed the threshold temperature T_T ($^\circ\text{C}$) from -8.0 to 0°C at an 0.5°C interval and obtained the correlation coefficients with the melt thickness during three periods: 1950–2020, 1958–2020, and 1979–2020 (Figure 5d). Figure 5 shows the relationship between melt thickness per year and PDH at the T_T of -4.5°C with the best correlation coefficient ($r = 0.68$, $p < 0.001$ in Figure 5a; $r = 0.69$, $p < 0.001$ in Figure 5b; and $r = 0.79$, $p < 0.001$ in Figure 5c). The period from 1979 to 2020 shows the best correlation. Nevertheless, all three periods show significant positive correlation coefficients. The threshold value of significantly below 0°C could be attributed to a bias in the ERA5 temperature. The significant positive correlation between melt thickness and PDH suggests that the interannual variability of melt thickness is also consistent with the summer mean temperature at the SE-Dome site. Thus, we conclude that the melt thickness may be a proxy for the summer mean temperature.

High MFPs were found in 1927 and 1889 when ERA5 data is not available (Figure 4d). During most summers of the 20th and 21st centuries, surface melting seldom occurred in highland dry snow regions of the GrIS (Keegan et al., 2014). In 1889, the widespread melting that extended inland occurred because of unusual warming and reduced albedo by black carbon from a remote forest fire (Keegan et al., 2014). The MLs formed by the 1889 melt event are also detected in other ice cores: for example, summit, NEEM, ACT-3, and D4 cores (Figure 1a; Keegan et al., 2014). As described in Chylek et al. (2006), the period from 1920 to 1930 is a strongly warming decade in GrIS. Our results suggest that the summer of 1927 was exceptionally warm in this warming period. A ML from 1927 is also observed in the ACT-3 ice core (Figure 1a; Das, 2009), suggesting the 1927 surface melting event was extensive over the inland (at least in the southern and southeastern) GrIS. Westhoff et al. (2022) reported that three MLs were detected in the EGRIP ice core from 1800 to 1964, whose thicknesses are observed. The 1889 CE melt event consists of two MLs with a total of 8.5 mm thickness and the 1950 CE melt event, with a ML of 3.1 mm thickness. Our results show the 1889 CE event consists of two MLs with a total thickness of 40 mm and the 1950 CE event consists of two MLs with a total of 33 mm thickness. Comparing our results with Westhoff et al. (2022), we determine that the SE-Dome site is more likely to melt, and form MLs than the EGRIP in the northern GrIS.

Finally, we investigate the summer temperature trends at the SE-Dome site using ERA5 data and melt thickness from the SE-Dome II ice core. During periods between 1960 and 1969 with an average summer temperature of $-9.09 \pm 0.70^\circ\text{C}$, the average melt thickness per year is 1.8 ± 3.8 mm. Between 1845 and 1919, just before the strongly warming period of the 1920s, the average melt thickness per year is 1.8 ± 6.5 mm, suggesting the average summer temperature from 1845 to 1919 is almost the same as that of 1960–1969. The average summer temperature is $-8.28 \pm 0.93^\circ\text{C}$ from 2000 to 2020 when thick MLs have been formed at one melting event in the SE-Dome site. Thus, the summer temperature has increased by 0.81°C from 1845–1919 to 2000–2020. Buizert et al. (2018) use ice core reconstructions and transient climate model simulations (TraCE-21Ka) to provide seasonally resolved surface air temperatures. The summer temperatures have increased 1.5 – 1.8°C in the northern region (NEEM, NGRIP, EGRIP, Camp Century, and Hans Tausen), 1.4 and 1.7°C in the central region (Summit and ReCAP), and 1.1°C in the southern region (Dye-3) from 1800 to 2000 (Buizert et al., 2018). Hörhold et al. (2023) shows that the annual temperature for the decade spanning 2001–2011 is $1.5 \pm 0.4^\circ\text{C}$ warmer than the twentieth century in the north-central region. Although the period ranges are different, these results suggest that the summer temperature increase in the SE-Dome site is representative of the summer temperature trend in the southern GrIS. In addition, the northern region has a larger temperature gap than other regions such as southern SE-Dome site, not only in summer but also annually.

4. Summary

In this study, we observed melt features and measured bulk density, high-resolution density, electrical conductivity, tritium concentration, and H_2O_2 concentrations on an ice core drilled in the southeastern GrIS (SE-Dome). Five time horizons were determined using electrical conductivity, melt events, tritium concentration, and annual layers were counted using H_2O_2 data. The resulting time scale covers the period from 1799 to 2020 with an uncertainty of 0.5 years. An age scale with half-year uncertainty provides the basis for future reconstruction and discussion of high-quality proxies, such as aerosols, back to the preindustrial era.

This accurate time scale with high-resolution density data also provides an annually resolved snow accumulation rate for the period from 1800 to 2020 at the SE-Dome site. The accumulation rate shows no significant trend over the 221 year period, with an average of 1.04 ± 0.20 m w.e. year^{-1} regardless of Arctic warming. This trend is similar to the precipitation trend in the central-east and northeastern GrIS but disagrees with that seen in the southwestern GrIS (Mernild et al., 2015). This result suggests that the precipitation trends differ between the southeastern and southwestern GrIS. We determined that the precipitation trend in eastern GrIS may be affected by the cyclicity over the eastern GrIS. This new accumulation rate data set for the SE-Dome site will be particularly useful for validating climate models that show large discrepancies in simulated snow accumulation rates over the southeastern GrIS (Fettweis et al., 2020).

The frequency and thickness of refrozen MLs have on average increased at the SE-Dome with Arctic warming. Additionally, the time-integrated summer temperature anomaly positively correlates with the melt thickness per year. Exceptionally thick MLs are found in 1889 and 1927, indicating extensive melting events in the period when reanalysis data is not available. This study concludes that the accumulation trend is similar to that in the eastern

GrIS and the summer temperature trend is similar to that seen in the southern GrIS over the past 221 years at the SE-Dome site.

Data Availability Statement

The IceBridge MCoRDS L2 Ice Thickness v1 was provided by National Snow and Ice Data Center (Paden et al., 2010). The ERA5 reanalysis data were downloaded from the ECMWF server (Hersbach et al., 2020). The data used in this study are available in National Climatic Data Center, NOAA (<https://www.ncdc.noaa.gov/access/paleo-search/study/38404>), and also in Hokkaido University Collection of Scholarly and Academic papers, HUSCAP (<http://hdl.handle.net/2115/90286>).

Acknowledgments

The authors acknowledge Ms. Maki Nakata for the Tritium analysis. The paper was significantly improved as a result of comments by three anonymous referees, to whom we are greatly indebted. This study was supported by MEXT/JSPS KAKENHI Grant 18H05292, 23H00511, 23K18516, and the Arctic Challenge for Sustainability (ArCS II) Project, Program Grant JPMXD1420318865. This study was supported by National Institute of Polar Research (NIPR) through General Collaboration Project no. 3-8. SH is supported by MEXT/JSPS KAKENHI Grant 20H04305 and start-up funding from Nanjing University. SI is supported by MEXT/JSPS KAKENHI Grant 20K19961.

References

- Aizawa, T., Oshima, N., & Yukimoto, S. (2022). Contributions of anthropogenic aerosol forcing and multidecadal internal variability to mid-20th century Arctic cooling CMIP6/DAMIP multimodel analysis. *Geophysical Research Letters*, 49(4), e2021GL097093. <https://doi.org/10.1029/2021GL097093>
- Amino, T., Iizuka, Y., Matoba, S., Shimada, R., Oshima, N., Suzuki, T., et al. (2021). Annual and seasonal dust fluxes during 1960–2014 from a southeastern dome in GrIS. *Polar Science*, 27, 100599. <https://doi.org/10.1016/j.polar.2020.100599>
- Andersen, K. K., Svensson, A., Johnsen, S. J., Rasmussen, S. O., Bigler, M., Röthlisberger, R., et al. (2006). The GrIS ice core chronology 2005, 15–42 ka. Part 1: Constructing the time scale. *Quaternary Science Reviews*, 25(23–24), 3246–3257. <https://doi.org/10.1016/j.quascirev.2006.08.002>
- Anklin, M., Bales, R. C., Mosley-Thompson, E., & Steffen, K. (1998). Annual accumulation at two sites in northwest GrIS during recent centuries. *Journal of Geophysical Research*, 103(D22), 28775–28783. <https://doi.org/10.1029/98JD02718>
- Bales, R. C., Guo, Q., Shen, D., McConnell, J. R., Du, G., Burkhart, J. F., et al. (2009). Annual accumulation for GrIS updated using ice core data developed during 2000–2006 and analysis of daily coastal meteorological data. *Journal of Geophysical Research*, 114(D6), D06116. <https://doi.org/10.1029/2008JD011208>
- Buchardt, S. L., Clausen, H. B., Vinther, B. M., & Dahl-Jensen, D. (2012). Investigating the past and recent $\delta^{18}\text{O}$ -accumulation relationship seen in GrIS ice cores. *Climate of the Past*, 8(6), 2053–2059. <https://doi.org/10.5194/cp-8-2053-2012>
- Buizert, C., Keisling, B. A., Box, J. E., He, F., Carlson, A. E., Sinclair, G., & DeConto, R. M. (2018). GrIS-wide seasonal temperatures during the last deglaciation. *Geophysical Research Letters*, 45(4), 1905–1914. <https://doi.org/10.1002/2017GL075601>
- Burgess, E. W., Forster, R. R., Box, J. E., Mosley-Thompson, E., Bromwich, D. H., Bales, R. C., & Smith, L. C. (2010). A spatially calibrated model of annual accumulation rate on the GrIS Ice Sheet (1958–2007). *Journal of Geophysical Research*, 115(F2), F02004. <https://doi.org/10.1029/2009JF001293>
- Chylek, P., Dubey, M. K., & Lesins, G. (2006). GrIS warming of 1920–1930 and 1995–2005. *Geophysical Research Letters*, 33(11), L11707. <https://doi.org/10.1029/2006GL026510>
- Clausen, H. B., & Hammer, C. U. (1988). The Laki and Tambora eruptions as revealed in GrIS ice cores from 11 locations. *Annals of Glaciology*, 10, 16–22. <https://doi.org/10.3189/s0260305500004092>
- Clausen, H. B., Hammer, C. U., Hvidberg, C. S., Dahl-Jensen, D., Steffensen, J. P., Kipfstuhl, J., & Legrand, M. (1997). A comparison of the volcanic records over the past 4000 years from the GrIS Ice Core Project and Dye 3 GrIS ice cores. *Journal of Geophysical Research*, 102(C12), 26707–26723. <https://doi.org/10.1029/97jc00587>
- Das, S. B. (2009). NOAA/WDS Paleoclimatology – ACT1, ACT3, ACT4, ACT2 – Melt layer thickness. Greenland ACT ice cores melt layer stratigraphy [Dataset]. NOAA National Centers for Environmental Information. <https://doi.org/10.25921/0mbh-xf84>
- Fegyveresi, J. M., Alley, R. B., Muto, A., Orsi, A. J., & Spencer, M. K. (2018). Surface formation, preservation, and history of low-porosity crusts at the WAIS Divide site, West Antarctica. *The Cryosphere*, 12(1), 325–341. <https://doi.org/10.5194/tc-12-325-2018>
- Fettweis, X., Hofer, S., Krebs-Kanzow, U., Amory, C., Aoki, T., Berends, C. J., et al. (2020). GrSMBMIP: Intercomparison of the modelled 1980–2012 surface mass balance over the GrIS Ice Sheet. *The Cryosphere*, 14(11), 3935–3958. <https://doi.org/10.5194/tc-14-3935-2020>
- Frey, M. M., Bales, R. C., & McConnell, J. R. (2006). Climate sensitivity of the century-scale hydrogen peroxide (H₂O₂) record preserved in 23 ice cores from West Antarctica. *Journal of Geophysical Research*, 111(21), D21301. <https://doi.org/10.1029/2005JD006816>
- Fujita, K., Matoba, S., Iizuka, Y., Takeuchi, N., Tsumura, A., Kurosaki, Y., & Aoki, T. (2021). Physically based summer temperature reconstruction from melt layers in ice cores. *Earth and Space Science*, 8(7), e2020EA001590. <https://doi.org/10.1029/2020EA001590>
- Furukawa, R., Uemura, R., Fujita, K., Sjolte, J., Yoshimura, K., Matoba, S., & Iizuka, Y. (2017). Seasonal-scale dating of a shallow ice core from GrIS using oxygen isotope matching between data and simulation. *Journal of Geophysical Research: Atmospheres*, 122(20), 10873–10887. <https://doi.org/10.1002/2017JD026716>
- Gerber, T. A., Hvidberg, C. S., Rasmussen, S. O., Franke, S., Sinnl, G., Grinsted, A., et al. (2021). Upstream flow effects revealed in the East-GRIP ice core using Monte Carlo inversion of a two-dimensional ice-flow model. *The Cryosphere*, 15(8), 3655–3679. <https://doi.org/10.5194/tc-15-3655-2021>
- Gfeller, G., Fischer, H., Bigler, M., Schüpbach, S., Leuenberger, D., & Mini, O. (2014). Representativeness and seasonality of major ion records derived from NEEM firn cores. *The Cryosphere*, 8(5), 1855–1870. <https://doi.org/10.5194/tc-8-1855-2014>
- Graeter, K. A., Osterberg, E. C., Ferris, D. G., Hawley, R. L., Marshall, H. P., Lewis, G., et al. (2018). Ice core records of West GrIS melt and climate forcing. *Geophysical Research Letters*, 45(7), 3164–3172. <https://doi.org/10.1002/2017GL076641>
- Hammer, C. U. (1980). Acidity of polar ice cores in relation to absolute dating, past volcanism, and radio-echoes. *Journal of Glaciology*, 25(93), 359–372. <https://doi.org/10.3189/s0022143000015227>
- Hanna, E., McConnell, J., Das, S., Cappelen, J., & Stephens, A. (2006). Observed and modeled GrIS ice sheet snow accumulation, 1958–2003, and links with regional climate forcing. *Journal of Climate*, 19(3), 344–358. <https://doi.org/10.1175/jcli3615.1>
- Hersbach, H., Bell, B., Berrisford, P., Hirahara, S., Horányi, A., Muñoz-Sabater, J., et al. (2020). The ERA5 global reanalysis [Dataset]. Quarterly Journal of the Royal Meteorological Society, 146(730), 1999–2049. Retrieved from <https://cds.climate.copernicus.eu/cdsapp#!/dataset/reanalysis-era5-pressure-levels>

- Hörhold, M., Münch, T., Weißbach, S., Kipfstuhl, S., Freitag, J., Sasgen, I., et al. (2023). Modern temperatures in central-north GrIS warmest in past millennium. *Nature*, 613(7944), 503–507. <https://doi.org/10.1038/s41586-022-05517-z>
- Hori, A., Tayuki, K., Narita, H., Hondoh, T., Fujita, S., Kameda, T., et al. (1999). A detailed density profile of the Dome Fuji (Antarctica) shallow ice core by X-ray transmission method. *Annals of Glaciology*, 29, 211–214. <https://doi.org/10.3189/172756499781821157>
- Iizuka, Y., Matoba, S., Minowa, M., Yamasaki, T., Kawakami, K., Kakugo, A., et al. (2021). Ice core drilling and related observations at SE-Dome site, southeastern GrIS Ice Sheet. *Bulletin of Glaciological Research*, 39(0), 1–12. <https://doi.org/10.5331/bgr.21r01>
- Iizuka, Y., Matoba, S., Yamasaki, T., Oyabu, I., Kadota, M., & Aoki, T. (2016). Glaciological and meteorological observations at the SE-Dome site, southeastern GrIS Ice Sheet. *Bulletin of Glaciological Research*, 34, 1–10. <https://doi.org/10.5331/bgr.15R03>
- Iizuka, Y., Miyamoto, A., Hori, A., Matoba, S., Furukawa, R., Saito, T., et al. (2017). A firm densification process in the high accumulation dome of southeastern GrIS. *Arctic, Antarctic, and Alpine Research*, 49(1), 13–27. <https://doi.org/10.1657/AAAR0016-034>
- Iizuka, Y., Uemura, R., Fujita, K., Hattori, S., Seki, O., Miyamoto, C., et al. (2018). A 60 year record of atmospheric aerosol depositions preserved in a high-accumulation dome ice core, Southeast GrIS. *Journal of Geophysical Research: Atmospheres*, 123(1), 574–589. <https://doi.org/10.1002/2017JD026733>
- Kameda, T., Narita, H., Shoji, H., Nishio, F., Fujii, Y., & Watanabe, O. (1995). Melt features in ice cores from site J, southern GrIS: Some implications for summer climate since AD 1550. *Annals of Glaciology*, 21, 51–58. <https://doi.org/10.3189/S0260305500015597>
- Karlsson, N., Razik, S., Hörhold, M., Winter, A., Steinhage, D., Binder, T., & Eisen, O. (2020). Surface accumulation in Northern Central GrIS during the last 300 years. *Annals of Glaciology*, 61(81), 214–224. <https://doi.org/10.1017/aog.2020.30>
- Keegan, K. M., Albert, M. R., McConnell, J. R., & Baker, I. (2014). Climate change and forest fires synergistically drive widespread melt events of the GrIS Ice Sheet. *PNAS*, 111(22), 7964–7967. <https://doi.org/10.1073/pnas.1405397111>
- Kendall, M. G. (1975). *Rank correlation measures*. Charles Griffin.
- Khalzan, P., Sakai, A., & Fujita, K. (2022). Mass balance of four Mongolian glaciers: In-situ measurements, longterm reconstruction and sensitivity analysis. *Frontiers in Earth Science*, 9, 785306. <https://doi.org/10.3389/feart.2021.785306>
- Kohno, M., & Fujii, Y. (2002). Past 220 year bipolar volcanic signals: Remarks on common features of their source volcanic eruptions. *Annals of Glaciology*, 35, 217–223. <https://doi.org/10.3189/172756402781816807>
- Lazrus, A. L., Kok, G. L., Gitlin, S. N., Lind, J. A., & McLaren, S. E. (1985). Automated fluorimetric method for hydrogen peroxide in atmospheric precipitation. *Analytical Chemistry*, 57(4), 917–922. <https://doi.org/10.1021/ac00281a031>
- Mann, H. B. (1945). Non-parametric tests against trend. *Econometrica*, 13(3), 245–259. <https://doi.org/10.2307/1907187>
- Mernild, S. H., Hanna, E., McConnell, J. R., Sigl, M., Beckerman, A. P., Yde, J. C., et al. (2015). GrIS precipitation trends in a long-term instrumental climate context (1890–2012): Evaluation of coastal and ice core records. *International Journal of Climatology*, 35(2), 303–320. <https://doi.org/10.1002/joc.3986>
- Miège, C., Forster, R., Box, J., Burgess, E., McConnell, J., Pasteris, D., & Spikes, V. (2013). Southeast GrIS high accumulation rates derived from firn cores and ground-penetrating radar. *Annals of Glaciology*, 54(63), 322–332. <https://doi.org/10.3189/2013AoG63A358>
- Mojtabavi, S., Wilhelms, F., Cook, E., Davies, S. M., Sinnl, G., Jensen, S., et al. (2020). A first chronology for the East GrIS Ice-core Project (EGRIP) over the Holocene and last glacial termination. *Climate of the Past*, 16(6), 2359–2380. <https://doi.org/10.5194/cp-16-2359-2020>
- Moore, J. C., & Paren, J. G. (1987). A new technique for dielectric logging of Antarctic ice cores. *Journal of Physics (Paris)*, 48(C1), 155–160. <https://doi.org/10.1051/jphyscol:1987123>
- Morlighem, M., Williams, C. N., Rignot, E., An, L., Arndt, J. E., Bamber, J. L., et al. (2017). BedMachine v3: Complete bed topography and ocean bathymetry mapping of GrIS from multibeam echo sounding combined with mass conservation. *Geophysical Research Letters*, 44, 11051–11061. <https://doi.org/10.1002/2017GL074954>
- Mosley-Thompson, E., McConnell, J. R., Bales, R. C., Li, Z., Lin, P. N., Steffen, K., et al. (2001). Local to regional-scale variability of annual net accumulation on the GrIS ice sheet from PARCA cores. *Journal of Geophysical Research*, 106(D24), 33839–33851. <https://doi.org/10.1029/2001JD900067>
- NEEM Community Members. (2013). Eemian interglacial reconstructed from a GrIS folded ice core. *Nature*, 493(7433), 489–494. <https://doi.org/10.1038/nature11789>
- Neff, W., Compo, G. P., Ralph, F. M., & Shupe, M. D. (2014). Continental heat anomalies and the extreme melting of the GrIS ice surface in 2012 and 1889. *Journal of Geophysical Research: Atmospheres*, 119(11), 6520–6536. <https://doi.org/10.1002/2014jd021470>
- Nghiem, S. V., Hall, D. K., Mote, T. L., Tedesco, M., Albert, M. R., Keegan, K., et al. (2012). The extreme melt across the GrIS ice sheet in 2012. *Geophysical Research Letters*, 39(20), L20502. <https://doi.org/10.1029/2012GL053611>
- Otosaka, I. N., Shepherd, A., Casal, T. G., Coccia, A., Davidson, M., Di Bella, A., et al. (2020). Surface melting drives fluctuations in airborne radar penetration in West Central GrIS. *Geophysical Research Letters*, 47(17), e2020GL088293. <https://doi.org/10.1029/2020GL088293>
- Paden, J., Li, J., Leuschen, C., Rodriguez-Morales, F., & Hale, R. (2010). IceBridge MCoRDS L2 ice thickness, Version 1 [Dataset]. NASA National Snow and Ice Data Center Distributed Active Archive Center. <https://doi.org/10.5067/GDQOCUCVTE2Q>
- Paterson, W. S. B. (2006). *The physics of glaciers* (4th ed.).
- Pfeffer, W. T., & Humphrey, N. F. (1998). Formation of ice layers by infiltration and refreezing of meltwater. *Annals of Glaciology*, 26, 83–91. <https://doi.org/10.3189/1998aog26-1-83-91>
- Porter, C., Morin, P., Howat, I., Noh, M.-J., Bates, B., Peterman, K., et al. (2018). ArcticDEM [Dataset]. V1, Harvard Data verse. <https://doi.org/10.7910/DVN/OHHUKH>
- Qiao, J., Colgan, W., Jakobs, G., & Nielsen, S. (2021). High-resolution tritium profile in an ice core from Camp Century, GrIS. *Environmental Science & Technology*, 55(20), 13638–13645. <https://doi.org/10.1021/acs.est.1c01975>
- Rasmussen, S. O., Seierstad, I. K., Andersen, K. K., Bigler, M., Dahl-Jensen, D., Johnsen, S. J., et al. (2008). Synchronization of the NGRIP, GRIP, and GISP2 ice cores across MIS 2 and paleoclimatic implications. *Quaternary Science Reviews*, 27(1–2), 18–28. <https://doi.org/10.1016/j.quascirev.2007.01.016>
- Sakai, A., Nuimura, T., Fujita, K., Takenaka, S., Nagai, H., & Lamsal, D. (2015). Climate regime of Asian glaciers revealed by GAMDAM glacier inventory. *The Cryosphere*, 9(3), 865–880. <https://doi.org/10.5194/tc-9-865-2015>
- Serreze, M. C., & Francis, J. A. (2006). The Arctic amplification debate. *Climatic Change*, 76(3–4), 241–264. <https://doi.org/10.1007/s10584-005-9017-y>
- Sigg, A., & Neftel, A. (1988). Seasonal variations in hydrogen peroxide in polar ice cores. *Annals of Glaciology*, 10, 157–162. <https://doi.org/10.3189/S0260305500004353>
- Sigl, M., Fudge, T. J., Winstrup, M., Cole-Dai, J., Ferris, D., McConnell, J. R., et al. (2016). The WAIS Divide deep ice core WD2014 chronology – Part 2: Annual-layer counting (0–31 ka BP). *Climate of the Past*, 12(3), 769–786. <https://doi.org/10.5194/cp-12-769-2016>
- Sigl, M., McConnell, J. R., Layman, L., Maselli, O., McGwire, K., Pasteris, D., et al. (2013). A new bipolar ice core record of volcanism from WAIS Divide and NEEM and implications for climate forcing of the last 2000 years. *Journal of Geophysical Research: Atmospheres*, 118(3), 1151–1169. <https://doi.org/10.1029/2012jd018603>

- Sinnl, G., Winstrup, M., Erhardt, T., Cook, E., Jensen, C. M., Svensson, A., et al. (2022). A multi-ice-core, annual-layer-counted GrIS ice-core chronology for the last 3800 years: GICC21. *Climate of the Past*, *18*(5), 1125–1150. <https://doi.org/10.5194/cp-18-1125-2022>
- Steen-Larsen, H. C., Masson-Delmotte, V., Sjolte, J., Johnsen, S. J., Vinther, B. M., Bréon, F. M., et al. (2011). Understanding the climatic signal in the water stable isotope records from the NEEM shallow firn/ice cores in northwest GrIS. *Journal of Geophysical Research*, *116*(D6), 6108. <https://doi.org/10.1029/2010JD014311>
- Svensson, A., Andersen, K. K., Bigler, M., Clausen, H. B., Dahl-Jensen, D., Davies, S. M., et al. (2008). A 60000 year Greenland stratigraphic ice core chronology. *Climate of the Past*, *4*(1), 47–57. <https://doi.org/10.5194/cp-4-47-2008>
- Trusel, L. D., Das, S. B., Osman, M. B., Evans, M. J., Smith, B. E., Fettweis, X., et al. (2018). Nonlinear rise in GrIS runoff in response to post-industrial arctic warming. *Nature*, *564*(7734), 104–108. <https://doi.org/10.1038/s41586-018-0752-4>
- van den Broeke, M. R., Enderlin, E. M., Howat, I. M., Kuipers Munneke, P., Noël, B. P. Y., van de Berg, W. J., et al. (2016). On the recent contribution of the GrIS ice sheet to sea level change. *The Cryosphere*, *10*(5), 1933–1946. <https://doi.org/10.5194/tc-10-1933-2016>
- Vinther, B. M., Jones, P. D., Briffa, K. R., Clausen, H. B., Andersen, K. K., Dahl-Jensen, D., & Johnsen, S. J. (2010). Climatic signals in multiple highly resolved stable isotope records from GrIS. *Quaternary Science Reviews*, *29*(3–4), 522–538. <https://doi.org/10.1016/j.quascirev.2009.11.002>
- Weinhart, A. H., Kipfstuhl, S., Hörhold, M., Eisen, O., & Freitag, J. (2021). Spatial distribution of crusts in Antarctic and GrIS snowpacks and implications for snow and firn studies. *Frontiers in Earth Science*, *9*, 630070. <https://doi.org/10.3389/feart.2021.630070>
- Westhoff, J., Sinnl, G., Svensson, A., Freitag, J., Kjær, H. A., Vallelonga, P., et al. (2022). Melt in the GrIS EastGRIP ice core reveals Holocene warm events. *Climate of the Past*, *18*(5), 1011–1034. <https://doi.org/10.5194/cp-18-1011-2022>
- Wilhelms, F., Kipfstuhl, J., Miller, H., Heinloth, K., & Firestone, J. (1998). Precise dielectric profiling of ice cores: A new device with improved guarding and its theory. *Journal of Glaciology*, *44*(146), 171–174. <https://doi.org/10.3189/s002214300000246x>
- Wolff, E. W. (2000). Electrical stratigraphy of polar ice cores: Principles, methods, and findings. In T. Hondoh (Ed.), *Physics of ice core records* (pp. 155–171). Hokkaido University Press.

References From the Supporting Information

- Hattori, S., Iizuka, Y., Alexander, B., Ishino, S., Fujita, K., Zhai, S., et al. (2021). Isotopic evidence for acidity-driven enhancement of sulfate formation after SO₂ emission control. *Science Advances*, *7*(19), eabd4610. <https://doi.org/10.1126/sciadv.abd4610>
- Mojtabavi, S., Wilhelms, F., Cook, E., Davies, S. M., Sinnl, G., Skov Jensen, M., et al. (2020a). Specific conductivity measured with the dielectric profiling (DEP) technique on the EGRIP ice core, 13.77–1383.84 m depth [Dataset]. PANGAEA. <https://doi.org/10.1594/PANGAEA.919313>
- Mojtabavi, S., Wilhelms, F., Cook, E., Davies, S. M., Sinnl, G., Skov Jensen, M., et al. (2020b). Specific conductivity measured with the dielectric profiling (DEP) technique on the NGRIP1 ice core (down to 1371.69 m depth) [Dataset]. PANGAEA. <https://doi.org/10.1594/PANGAEA.922191>
- Wang, K., Hattori, S., Lin, M., Ishino, S., Alexander, B., Kamezaki, K., et al. (2021). Isotopic constraints on atmospheric sulfate formation pathways in the Mt. Everest region, southern Tibetan Plateau. *Atmospheric Chemistry and Physics*, *21*(10), 8357–8376. <https://doi.org/10.5194/acp-21-8357-2021>

[Journal of Geophysical Research Atmosphere]

Supporting Information for

[SE-Dome II ice core dating with half-year precision: Increasing melting events from 1799 to 2020 in southeastern Greenland]

[Kaoru Kawakami¹, Yoshinori Iizuka¹, Mahiro Sasage², Mai Matsumoto², Takeshi Saito¹, Akira Hori³, Sakiko Ishino⁴, Shuji Fujita^{5,6}, Koji Fujita⁷, Keita Takasugi³, Takumi Hatakeyama⁸, Saaya Hamamoto⁷, Akihisa Watari^{1,2}, Nao Esashi⁷, Miu Otsuka^{1,2}, Ryu Uemura⁷, Kazuho Horiuchi⁸, Masahiro Minowa¹, Shohei Hattori⁹, Teruo Aoki⁵, Motohiro Hirabayashi⁵, Kenji Kawamura^{5,6,10}, Sumito Matoba¹]

[1 Institute of Low Temperature Science, Hokkaido University, Sapporo, Japan

2 Graduate School of Environmental Science, Hokkaido University, Sapporo, Japan

3 Kitami Institute of Technology, Kitami, Japan

4 Institute of Nature and Environmental Technology, Kanazawa University, Kanazawa, Japan

5 National Institute of Polar Research, Tokyo 190-8518, Japan

6 Department of Polar Science, The Graduate University of Advanced Studies, SOKENDAI, Tokyo 190-8518, Japan

7 Graduate School of Environmental Studies, Nagoya University, Nagoya, Japan

8 Hirosaki University, Hirosaki, Japan

9 International Center for Isotope Effects Research, School of Earth Sciences and Engineering, Nanjing University, Nanjing, China

10 Japan Agency for Marine Science and Technology, Yokosuka 237-0061, Japan]

Contents of this file

TextS1

Figures S1 to S8

Text S1. Assumption for timing of minima and maxima in H₂O₂

The SE-Dome II ice core is half-annually dated by assuming that minima and maxima in H₂O₂ concentration correspond to mid-winter and mid-summer, respectively. This assumption is based on the fact that atmospheric H₂O₂ is predominantly produced via photochemistry (e.g., Frey et al., 2006; Gfeller et al., 2014). Support for this assumption comes from modeled monthly atmospheric H₂O₂ mixing ratios, averaged within the area where air mass reaching the SE-Dome travels within 3 days (longitude: 70°W to 0°, latitude: 55 to 80°N) taken from five outputs for different years (1960, 1973, 1986, 1999, and 2013) for the GEOS-Chem global chemistry transport model (Figure S5; Hattori et al. 2021, Wang et al., 2021). This suggests that H₂O₂ is minimized between December and January and maximized between June and July. Taken together with the fact that H₂O₂ production is induced by photochemistry, we therefore tie winter and summer solstice to the H₂O₂ minimum and maximums, respectively.

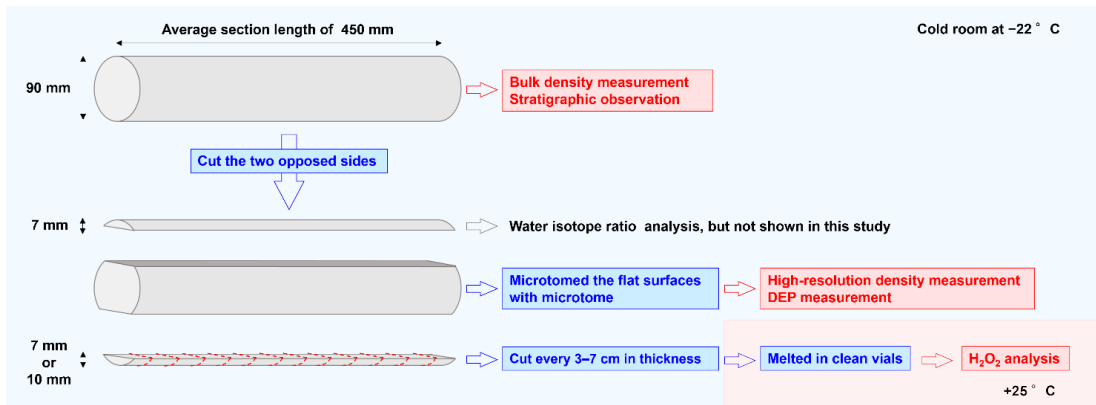


Figure S1. Cutting plan for the SE-Dome II ice core.

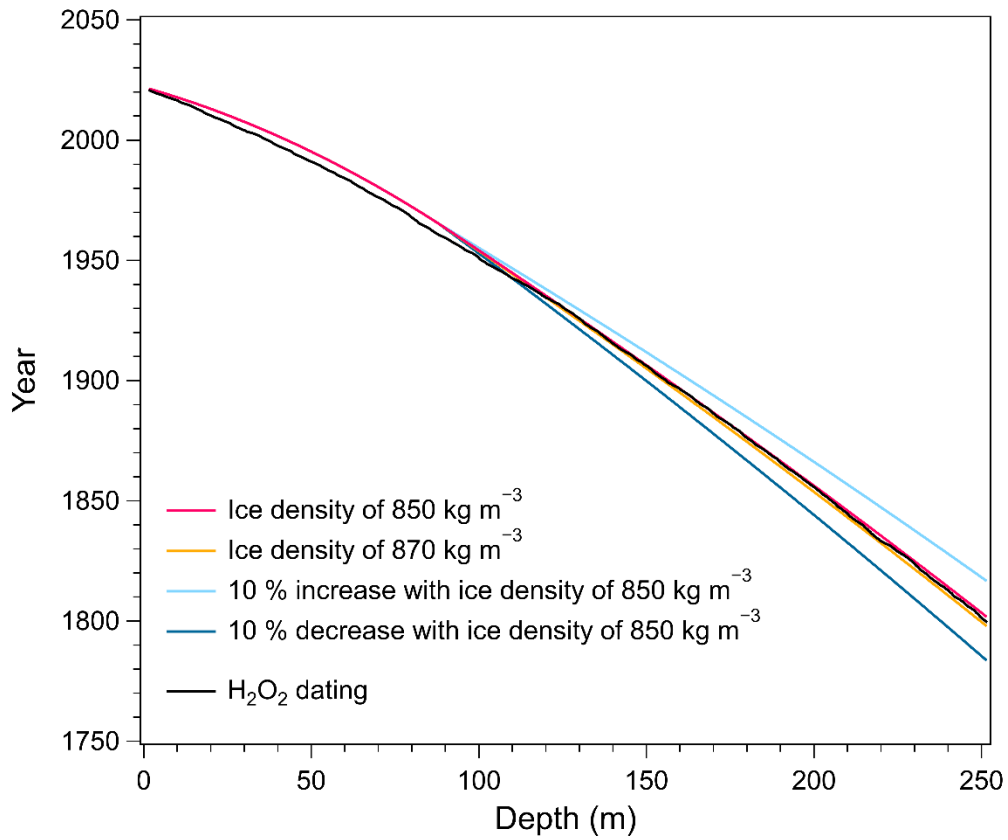


Figure S2. Depth vs age for SE-Dome II ice core corrected for annual layer thickness. The magenta and orange lines show the case with a density of 850 kg m^{-3} or 870 kg m^{-3} after closed-off depth. The light blue and dark blue lines show the case with an increase or decrease by 10% of annual accumulation rate. The black line show the actual dating in this study.

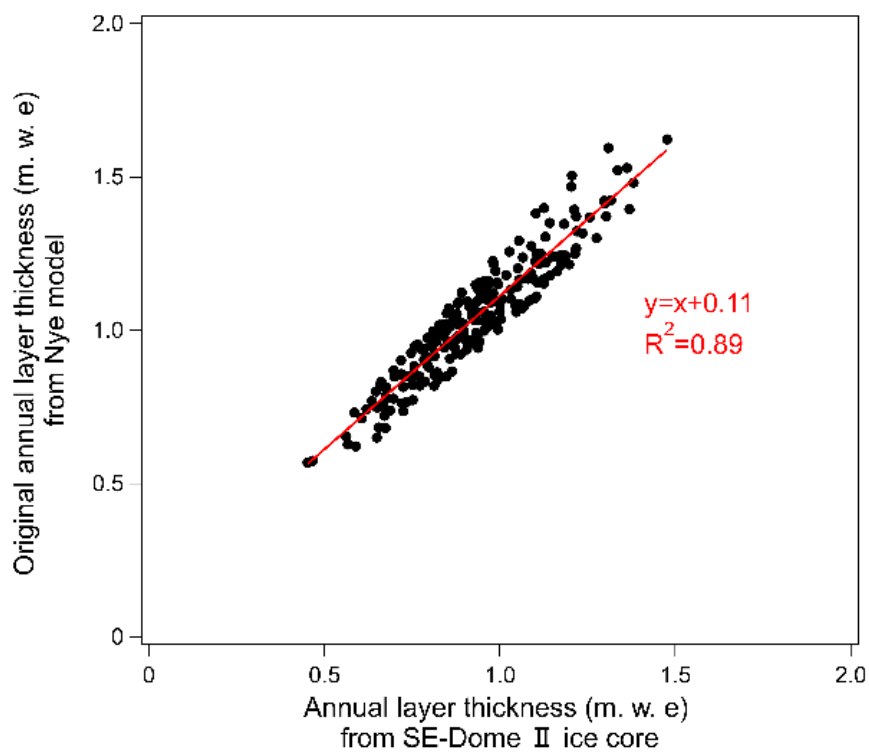


Figure S3. The relationship between annual layer thickness from SE-Dome II ice core and converted annual layer thickness by Nye model.

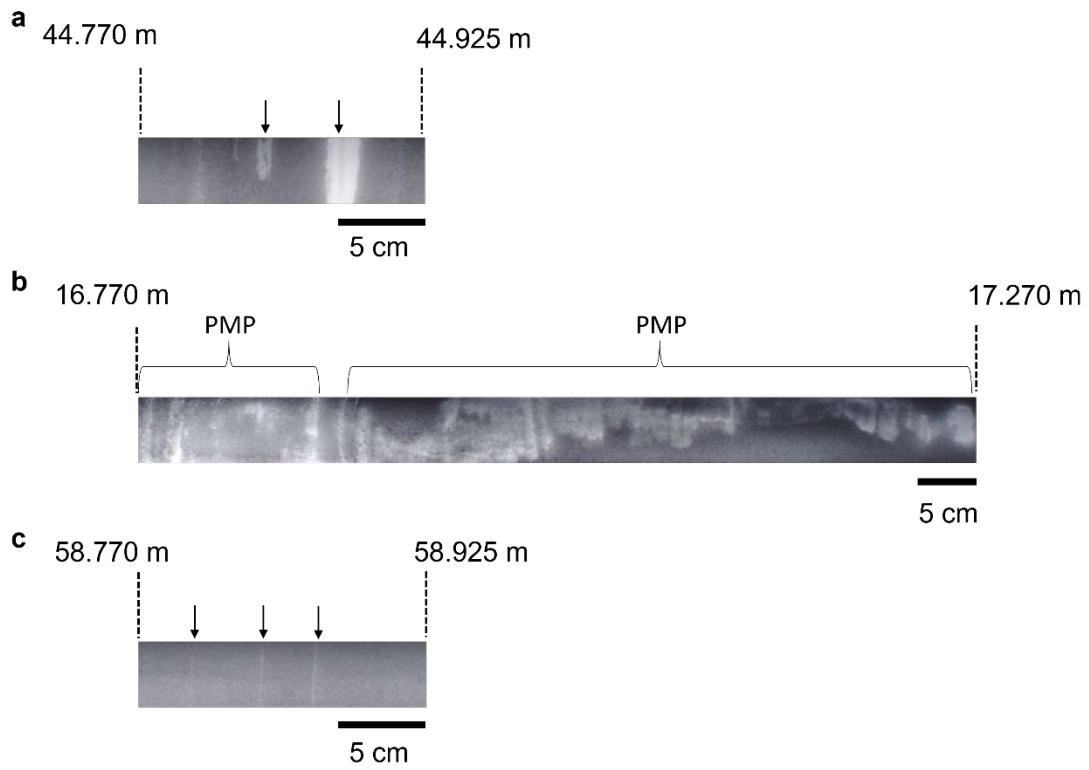


Figure S4. Examples of (a) melt layers (MLs) (> 1 mm), (b) percolated melt pipes (PMPs) (> 1 mm), and (c) melt crusts (MCs) (≤ 1 mm).

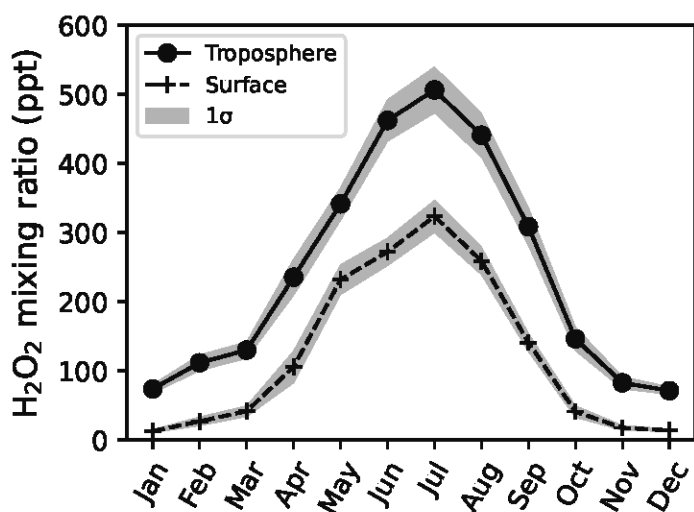


Figure S5. The seasonality of the atmospheric H₂O₂ mixing ratio simulated by the GEOS-Chem global chemistry transport model (version 12.5; see Hattori et al. (2021) and Wang et al. (2021) for details). The circle and cross plots show tropospheric and surface layer H₂O₂ mixing ratios averaged within the area where the air mass reaching the SE-Dome travels within 3 days (longitude: 70°W to 0°, latitude: 55 to 80°N). The shadows are standard deviation estimated from the five models for different years: 1960, 1973, 1986, 1999, and 2013.

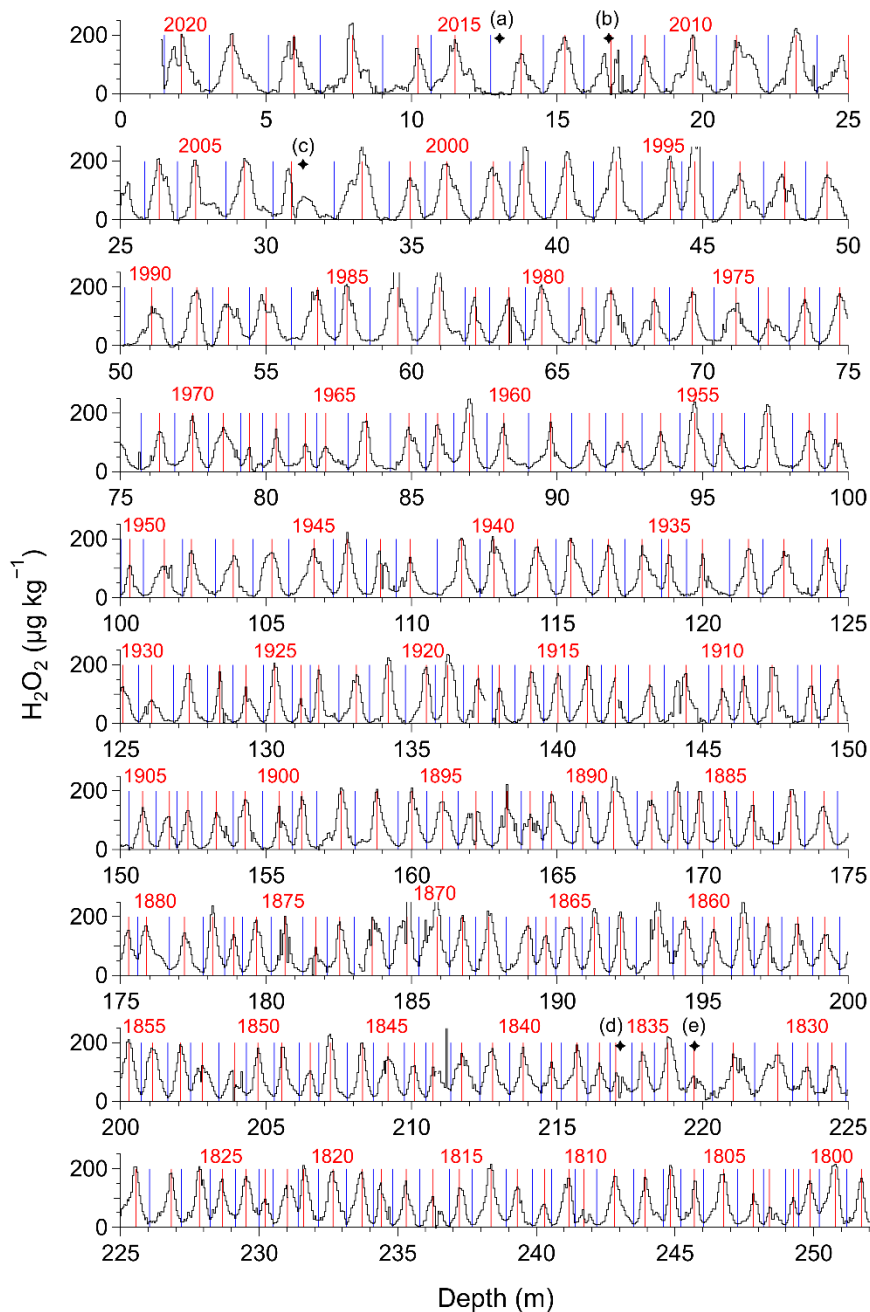


Figure S6. Depth profiles of H_2O_2 concentrations. The blue and red lines show the minimal and maximal H_2O_2 peaks in each year, which are considered to correspond to mid-winter and mid-summer. Low H_2O_2 concentrations disrupting the seasonal cycle are detected due to (a) the high dust flux from the eruption of Mt. Bardarbunga in Iceland in the autumn of 2014 (Amino et al. 2021), (b) the extreme melt event in 2012, (c) high dust concentration in 2003 (Amino et al., 2021), (d) the eruption of Mt. Cosigüina in Nicaragua in 1836, (e) the eruption of Mt. Babuyan in Philippine in 1833.

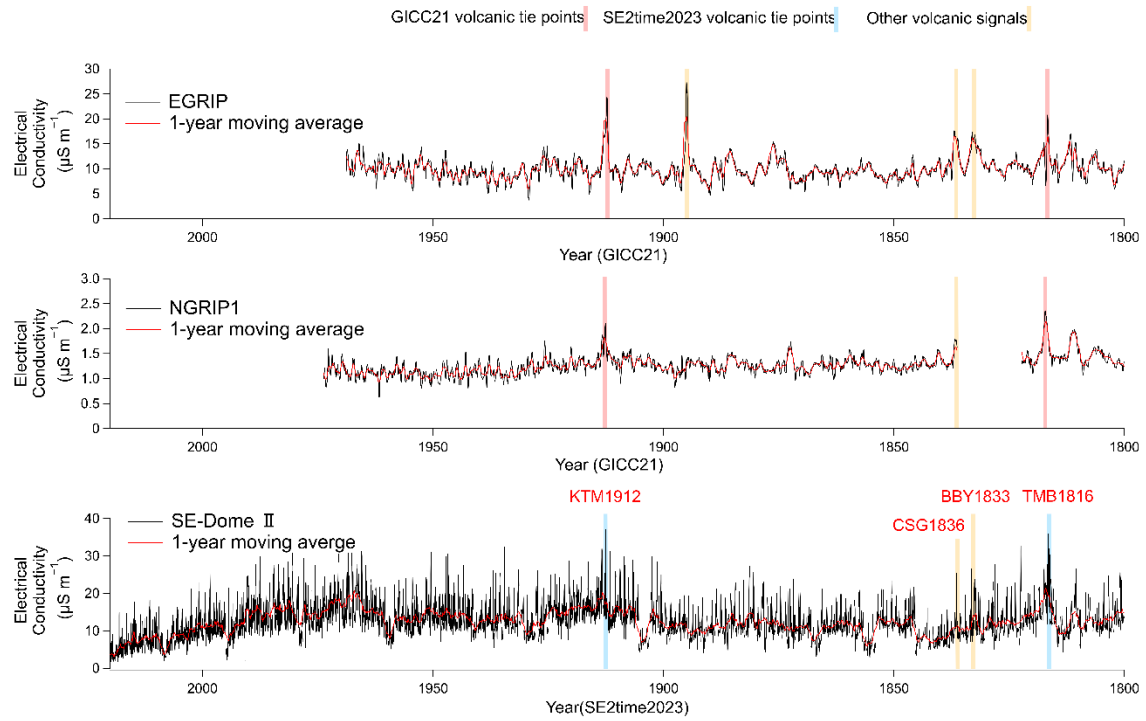


Figure S7. The age profiles of electrical conductivities from EGRIP (Mojtabavi et al., 2020a), NGRIP1 (Mojtabavi et al., 2020b), SE-Dome II ice core. 'KTM1912', 'CSG1836', 'BBY1833', and 'TMB1816' indicate the eruption events in 1912, 1836, 1833, and 1816.

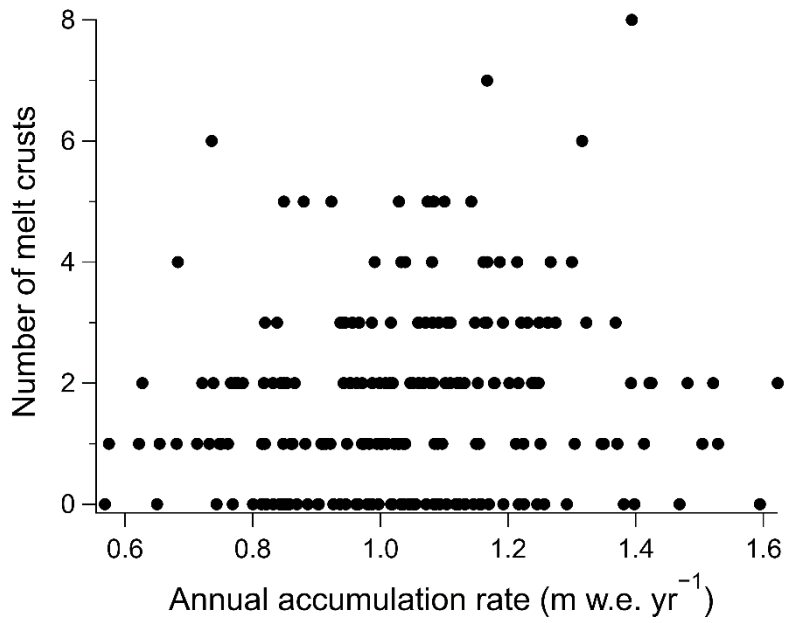


Figure S8. The relationship between the annual accumulation rate from the SE-Dome II ice core and the annual number of melt crusts from the SE-Dome II ice core from 1800–2020.